

Adaptive optics via pupil segmentation for high-resolution imaging in biological tissues

Na Ji¹, Daniel E Milkie² & Eric Betzig¹

Biological specimens are rife with optical inhomogeneities that seriously degrade imaging performance under all but the most ideal conditions. Measuring and then correcting for these inhomogeneities is the province of adaptive optics. Here we introduce an approach to adaptive optics in microscopy wherein the rear pupil of an objective lens is segmented into subregions, and light is directed individually to each subregion to measure, by image shift, the deflection faced by each group of rays as they emerge from the objective and travel through the specimen toward the focus. Applying our method to two-photon microscopy, we could recover near-diffraction-limited performance from a variety of biological and nonbiological samples exhibiting aberrations large or small and smoothly varying or abruptly changing. In particular, results from fixed mouse cortical slices illustrate our ability to improve signal and resolution to depths of 400 μm .

Since its invention centuries ago, light microscopy has evolved through many incarnations with distinct contrast mechanisms and hardware implementations. The fundamental motivation for its use, however, has remained the same: it can be used to resolve features that are not distinguishable by the naked eye. As a result, the push for higher resolution has been the focus of light microscopy development in recent years and several methods have been demonstrated to break the diffraction limit of conventional light microscopy¹. Despite all these efforts, one often-underappreciated fact remains: for many biological samples, diffraction-limited resolution is rarely achieved, even with high-end research microscopes. Ideal imaging performance of a light microscope requires the excitation and/or emission light to pass exclusively through samples with optical properties identical to those of the designed immersion medium. Any deviation causes optical distortions, known as aberrations, leading to the loss of signal, image fidelity and resolution^{2,3}. In practice, biological samples have inhomogeneous optical properties^{4,5}, so that images are increasingly degraded with increasing depth in biological tissues.

Similar challenges exist for a close relative of the optical microscope, the optical telescope. Light captured from remote stars must first traverse the earth's turbulent atmosphere, which imparts optical distortions that severely degrade image quality.

Methods that actively correct for such distortions, known collectively as adaptive optics (AO), have evolved over the past 40 years and now allow ground-based telescopes to obtain diffraction-limited images of extraterrestrial objects⁶. AO in astronomy is conceptually simple: a sensor placed near the imaging plane measures the distorted wavefront directly, and an active optical element, such as a deformable mirror, modifies this wavefront in a feedback loop to recover diffraction-limited performance⁷. However, AO in microscopy⁸ is made less straightforward by the difficulty in measuring the aberrated wavefront directly; after all, it is rarely possible to place a wavefront sensor within the specimen. Backscattered light from the specimen has been used for such direct wavefront sensing^{9,10}, but such methods convolve the possibly differing aberrations both to and from the image plane¹¹ and are further complicated by multiply scattered light. As a result, they have largely been confined to retinal imaging, in which light reflected by the retina overwhelms that from nearby tissues¹², or to relatively transparent samples such as zebrafish¹⁰. For most biological applications, especially *in vivo* tissue imaging, sample-induced aberration must be deduced indirectly. Based on an intuitive picture of optical focus formation, we developed an image-based AO method using rear pupil segmentation and demonstrated its utility in two-photon fluorescence microscopy by correcting aberrations from a variety of sources, from simple refractive-index mismatch to complex aberrations in 400- μm -thick mouse cortical slices.

RESULTS

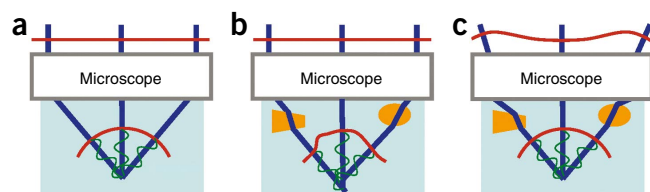
Adaptive optics using pupil segmentation

For two-photon fluorescence microscopy in thick tissues, the only aberrations that affect image quality are those experienced by the focused excitation light. Although this focus can be calculated from electromagnetic theory^{13–15} and deviations from its ideal, diffraction-limited form can be described mathematically in terms of an infinite series of aberration modes¹⁶, here we instead rely on a simple physical model of focus formation that leads to an intuitive AO algorithm for aberration correction.

In this model, a diffraction-limited focus is viewed to arise when all light rays entering the rear pupil of a microscope objective are bent to intersect at a common point with a common phase,

¹Janelia Farm Research Campus, Howard Hughes Medical Institute, Ashburn, Virginia, USA. ²Coleman Technologies, Inc., Unit 113, Chadds Ford, Pennsylvania, USA. Correspondence should be addressed to N.J. (jin@janelia.hhmi.org).

Figure 1 | A simple model of optical focus formation. (a) An ideal microscope converts a planar wavefront (top red line) to a converging spherical one (bottom red semicircle) in a sample of the design optical properties. Propagation vectors or ‘rays’ (blue), defined by the direction normal to the wavefront, converge at a common point and, being in phase, constructively interfere there to create an optimal focus. Green sinusoidal curves denote the phase variation along each ray. (b) Inhomogeneities (orange) in the refractive index of the sample change the directions and phases of the rays, leading to a distorted wavefront and an enlarged focal volume with lower peak intensity. (c) Controlling the input wavefront using an active optical element (not shown) can cancel these aberrations, recovering a diffraction-limited focus.



that is, a focus is a point of maximal constructive interference (Fig. 1a). Unanticipated refractive index inhomogeneities along the paths between the objective and the focal point deflect these rays, so they miss the focal point and shift their phases, so that they interfere with other rays less constructively (Fig. 1b). Using an active optical element optically conjugated to the rear pupil of the microscope objective, one could, in principle, steer all such rays individually back to the focal point and re-optimize their phases, effectively canceling all sample-induced aberrations and recover a diffraction-limited focus (Fig. 1c). Of course, it is not possible to individually manipulate an infinite continuum of rays, but it is possible to divide the active element into N subregions, each with an independently adjustable planar phase pattern, and thereby segment the rear pupil into N beamlets individually controllable for tilt and phase offset. As the complexity of the required corrective phase pattern across the rear pupil increases, more subregions are needed to achieve an accurate approximation. However, in this work we found that, for a wide variety of aberrations, $N < 100$ is usually sufficient to recover near diffraction-limited performance.

We present a schematic of our AO two-photon fluorescence microscope in **Supplementary Figure 1** and describe it in detail in Online Methods. We chose a reflective liquid-crystal phase-only spatial light modulator (SLM) rather than a deformable mirror as the active optical element because (i) with $1,920 \times 1,080$ pixels, it can be readily divided into hundreds of subregions, each with a smoothly varying linear phase ramp; (ii) subregions are truly independent and not mechanically coupled; (iii) corrective wavefronts of >100 wave amplitude can be generated via phase wrapping; and (iv) phase gradients of >60 wavelengths mm^{-1} can be produced, ~ 10 times greater than with popular large-stroke deformable mirrors^{17,18}. In the first step of our basic AO algorithm (**Supplementary Fig. 2** and **Supplementary Movie 1**), we acquire a reference image with the rear pupil fully illuminated. We then apply a binary phase pattern to all but one of the N subregions of the SLM, a pattern that causes the associated beamlets to be diffracted to and blocked by a field stop at an intermediate image plane, rendering them effectively ‘off’. We then acquire an image using the sole remaining ‘on’ beamlet. Any inhomogeneities along the path of the beamlet that deflect it from the ideal focal point are evidenced as a shift in this image relative to the reference image. For simple isolated objects, the shift can be determined from the shift in the centroid of the object, whereas for more complex samples, image correlation can be used. Regardless, once the shift is known, the deflection angle can be calculated, and an equal but opposite angle can be imparted to the beamlet by application of an appropriate phase ramp at the corresponding subregion of the SLM. This process is then repeated

with the other $N - 1$ subregions and beamlets, until all N beamlets intersect at a common focal point.

To bring all these beamlets in phase at this focal point, two different approaches can be used. In the first, deemed direct measurement, a reference beamlet is turned ‘on’, along with one of the other $N - 1$ beamlets. A series of P images is then acquired with different phases imparted to the second beamlet until the signal at the focal point is a maximum. This process is then repeated, using the same reference beamlet and, in turn, each of the remaining $N - 2$ beamlets. In the second approach, deemed phase reconstruction, the beam deflection angles determined above define an array of phase gradient measurements across the rear pupil, from which the phase itself can be extracted through an iterative algorithm¹⁹, similar to that used in the Shack-Hartmann wavefront sensor^{7,12,20}. Direct measurement yields a smaller residual wavefront error than does phase reconstruction for a given N but at the cost of PN more images that must be acquired (**Supplementary Fig. 3**). In either case, once the appropriate phase offsets are determined and applied, the AO algorithm is complete and, if N is sufficiently large, a diffraction-limited focus is achieved.

Adaptive optical correction for nonbiological samples

To test the magnitude and complexity of aberrations our microscope is capable of correcting, we introduced two examples of extreme aberration. In the first, we used a $20\times$, 1.0 numerical aperture (NA) water dipping objective to image a 500-nm -diameter fluorescent bead but omitted the water normally required between the objective and the sample, yielding extremely distorted images of the bead (Fig. 2a). After AO correction with direct phase measurement and 49 non-overlapping, independent subregions (N), the peak signal increased eightfold, and both the lateral and the axial full width at half maximum values approached their diffraction-limited values (Fig. 2b,c). The final resulting SLM pattern (after subtraction of system aberrations as discussed in Online Methods, **Supplementary Figs. 4,5** and **Supplementary Movie 2**) was clearly dominated by spherical aberration (Fig. 2d), and the peak-to-valley wavefront error of 20 wavelengths demonstrated our ability to accurately correct even very large aberrations. The correction remained valid over a $98 \times 98 \mu\text{m}$ field of beads in air (**Supplementary Fig. 6** and **Supplementary Movie 3**).

As a second example, we placed a 500-nm -diameter bead on the inside surface of a glass capillary tube, with water outside the tube and air inside, a geometry leading to substantial amounts of coma and astigmatism (Fig. 2e). After AO correction, the signal increased about 3.5-fold, and near-diffraction-limited performance was again attained (Fig. 2f,g), despite the fact that placement of the bead well away from the center line of the capillary tube resulted in a highly asymmetric wavefront (Fig. 2h).

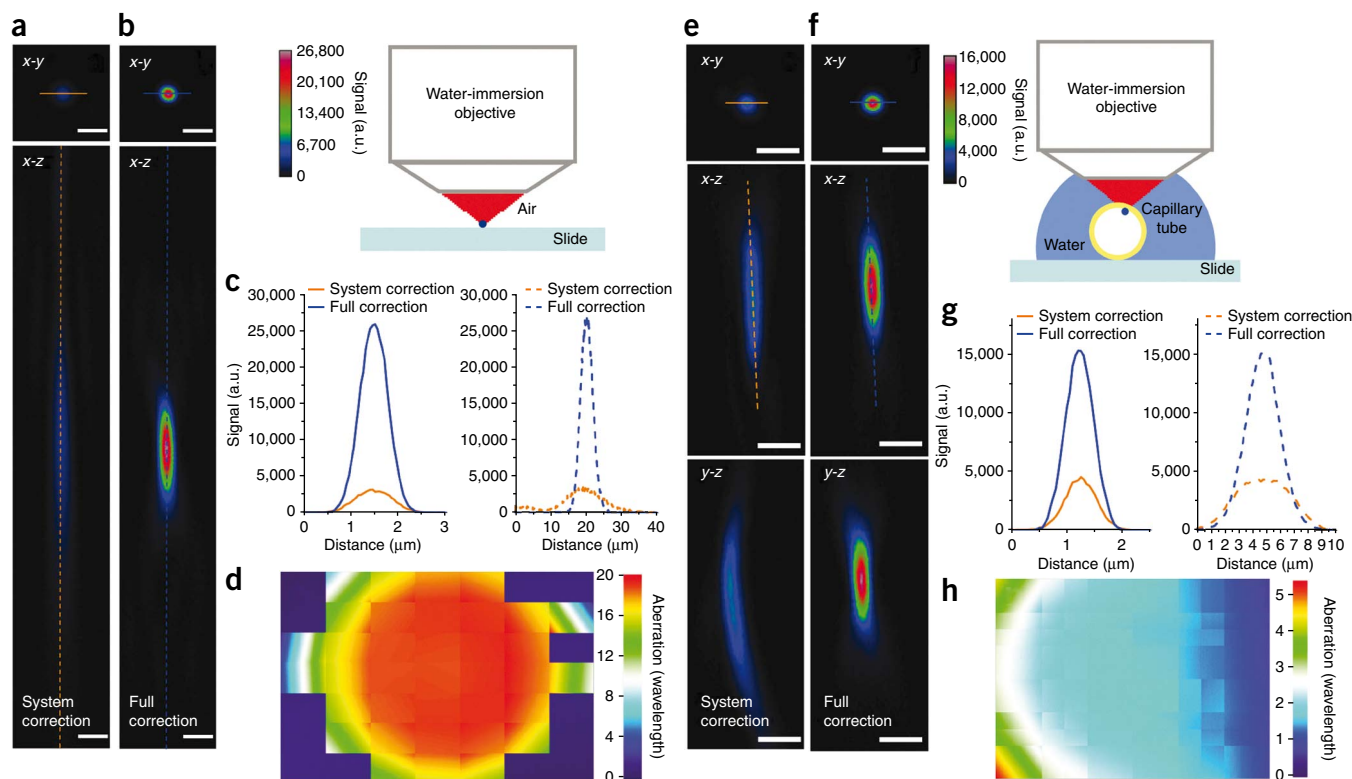


Figure 2 | Correction of aberrations caused by refractive index mismatch. **(a,b)** Lateral and axial images of a 500-nm fluorescent bead viewed in air using a water-dipping objective (schematic on the right in **b**), with correction for only system aberrations **(a)** or all aberrations **(b)**. **(c)** Signal profiles in the lateral (*x-y*) and axial (*x-z*) planes along the solid and dashed lines in **a** and **b**. **(d)** The final corrective wavefront, after subtraction of system aberrations, obtained with 49 independent subregions and direct phase measurement. Approximately 20 wavelengths of predominantly spherical aberration were corrected. Owing to the large refractive index mismatch at the exit of the objective, the peripheral subregions (purple) transmitted insufficient signal for accurate tilt and phase measurement and did not contribute markedly to the final images. **(e,f)** Images of a bead in an air-filled capillary tube in water (schematic on the right in **f**), with system aberration correction only **(e)** and full AO correction **(f)**. **(g)** Signal profiles in the lateral (*x-y*) and axial (*x-z*) planes along the solid and dashed lines in **e** and **f**. **(h)** The final corrective wavefront in units of excitation light wavelength (850 nm), after subtraction of system aberrations, obtained with 36 independent subregions and direct phase measurement. Scale bars, 2 μm .

Adaptive optical correction in biological samples

To test the effectiveness of our AO microscope in biological samples, we first imaged 1- μm -diameter beads through a 250- μm -thick fixed mouse cortical slice. With only the system aberration correction applied to the SLM, the excitation wavefront was so severely distorted by the brain slice that several ghost images of the bead appeared (Fig. 3a). To improve visibility, we increased the display gain fourfold (Fig. 3b), which highlighted the ghost images as well as the distorted axial image of the bead. After AO correction with direct phase measurement and 12 non-overlapping, independent subregions (Fig. 3c), the ghost images disappeared, the axial resolution improved, and the peak signal increased about fourfold (Fig. 3d,e). The lateral resolution, axial resolution and signal each varied as a function of N (Supplementary Fig. 7 and Online Methods).

Our approach as outlined so far faces considerable power limitations, as a single ‘on’ subregion will deliver at most $1/N$ of the available power to the sample in a beamlet of $\sim(N)^{-1/2}$ of the full NA of the objective. The result is a large focus of markedly reduced intensity (I) and, for two-photon excitation, an even more drastic reduction in peak signal (S) as $S \propto |I|^2$. Remediation measures we used include increasing the laser power and pixel integration time, and concentrating the light at the ‘on’ subregion using a $2\times$ beam reducer and a pair of beam-steering mirrors (Supplementary Fig. 1b).

Despite these measures, power still sets a practical limit on the number of beam deflection measurements, and hence the complexity of the correction we can provide, when the rear pupil is divided into N non-overlapping subregions, only one of which is turned on at a time (termed the independent mask approach). An alternative formulation leading to higher N involves turning on contiguous groups of subregions in a series of overlapping masks (Online Methods and Supplementary Fig. 8), with each mask covering a fraction, $1/M$, of the rear pupil area markedly larger than that of any single subregion, thereby producing a much more intense focus (termed the overlapping mask approach). We measured the beam deflection and phase offset for each mask as described above and applied different masks until each subregion was sampled by a unique set of masks, leading to a unique corrective phase in each subregion.

We illustrate this approach in Figure 3f–j: a pair of 1- μm -diameter beads imaged through a 250- μm -thick fixed mouse cortical slice yielded a pair of ghost images and poor axial resolution before AO correction (Fig. 3f,g) but no ghost images, diffraction-limited axial confinement and fourfold greater signal after application of this overlapping mask algorithm. The complex corrective wavefront (Fig. 3j) was densely sampled with 81 subregions, despite the fact that $1/9$ of the rear pupil was illuminated by each mask. Of course, for a given number of subregions, the independent

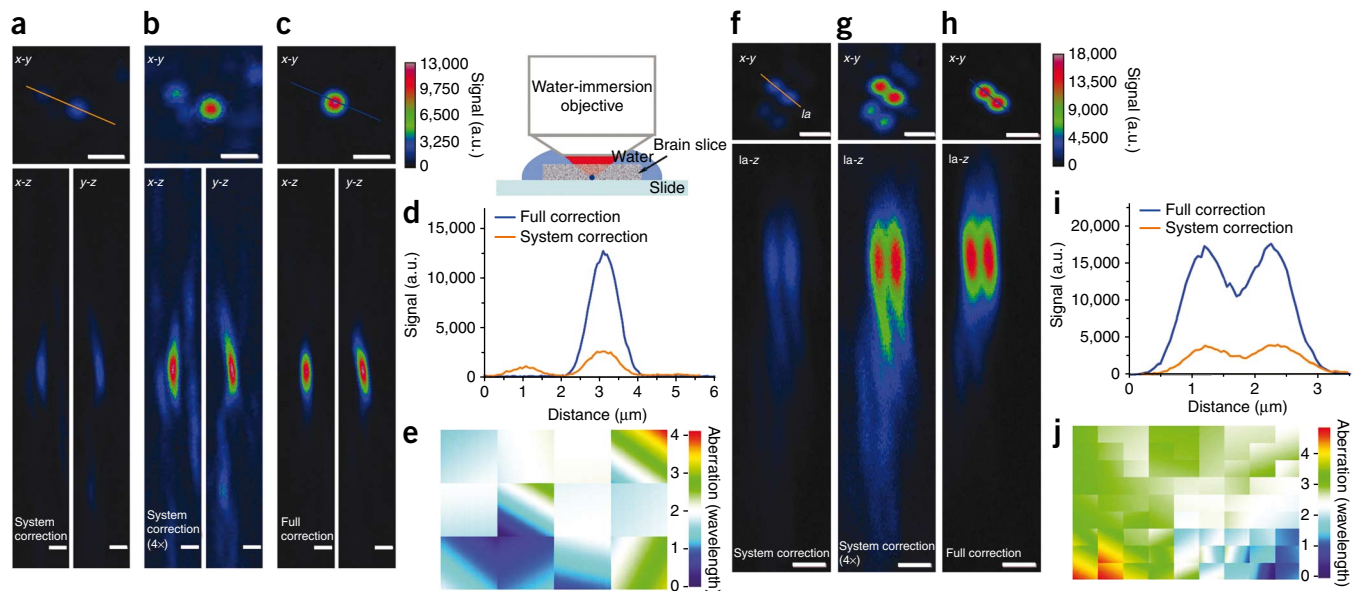


Figure 3 | Correction of aberrations induced by 250- μm -thick fixed mouse brain slices. (a–c) Experiment schematic is shown on the right in c. Lateral (x–y) and axial (x–z and y–z) images of a single bead under a brain slice, with only system correction applied (a), with a fourfold increase in display gain (b) and after full AO correction (c). (d) Lateral intensity profiles along the orange and blue lines in a and c. (e) The final corrective wavefront, after subtraction of system aberrations, using 12 independent subregions and direct phase measurement. (f,g) Lateral (x–y) and axial (la–z) images of a pair of 1- μm beads with only system correction applied. Display gain is increased fourfold in g relative to that in f. (h) Images of the same bead pair after full AO correction. (i) Lateral intensity profiles along the orange and blue lines in f and h. (j) The final corrective wavefront, in units of excitation light wavelength (850 nm), using the overlapping mask algorithm with 72 masks, each covering 1/9 of the rear pupil area, leading to 81 subregions of unique phase. Scale bars, 2 μm .

approach outperforms the overlapping mask approach, owing to residual coupling between the subregions. However, for a given mask area, or equivalently, a given laser power, implementation of overlapping masks allows many more subregions to be used and thus often leads to superior correction.

Yet another approach whereby an aberrated wavefront can be measured on a scale smaller than the size of a single ‘on’

subregion, involves moving the subregion in discrete steps smaller than the subregion itself (a special case of overlapping masks; **Supplementary Fig. 8d**) and measuring the beam deflection, and thus the phase gradient, at each step. Phase reconstruction^{19,20} can then be used to determine the optimal phase offset at each measurement point and combined with the gradient data to determine the plane of best fit to the aberrated wavefront in the region

centered at each measurement point. We compared this procedure, termed stepped overlap, to the independent method, using either measured or reconstructed phase (**Fig. 4**). In each case, we imaged the same 1- μm fluorescent bead under the same 250- μm -thick fixed cortical brain slice using ‘on’ masks of identical size (1/16 of the total pupil area). The 4 \times 4 independent mask

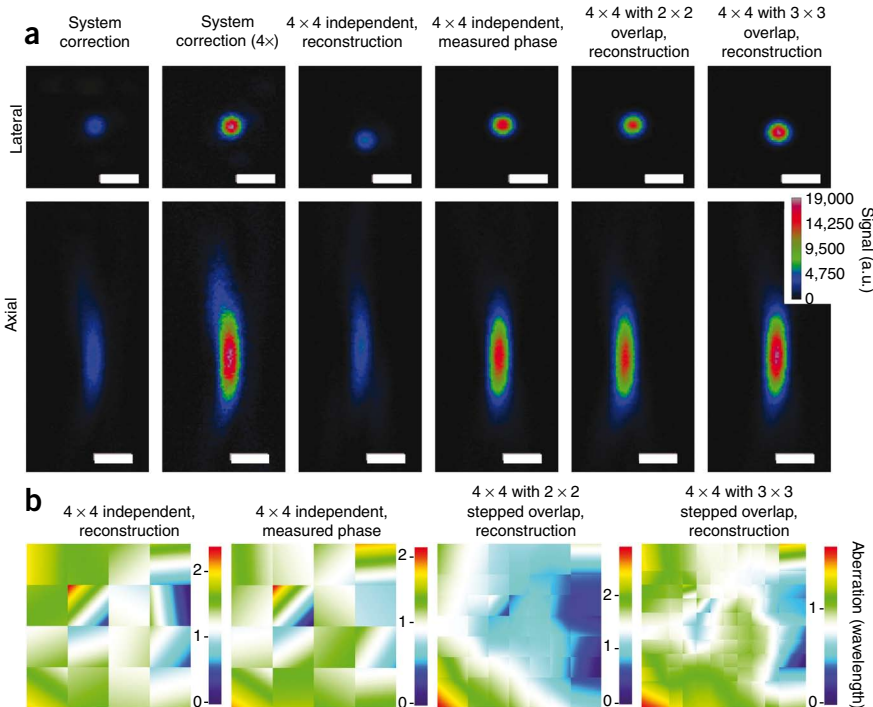


Figure 4 | AO correction on a 1- μm diameter bead under a 250- μm fixed brain slice, using different variations of our pupil segmentation algorithm.

(a) Lateral and axial images of the bead obtained with (left to right): system aberration correction only; system aberration correction with 4 \times display gain; 4 \times 4 independent subregions with reconstructed phase; 4 \times 4 independent subregions with measured phase; 4 \times 4 stepped overlap with 2 \times 2 steps and phase reconstruction; and 4 \times 4 stepped overlap with 3 \times 3 steps and phase reconstruction. Scale bars, 2 μm . (b) Final corrective wavefronts in units of excitation light wavelength (850 nm) after subtraction of system aberrations as indicated.

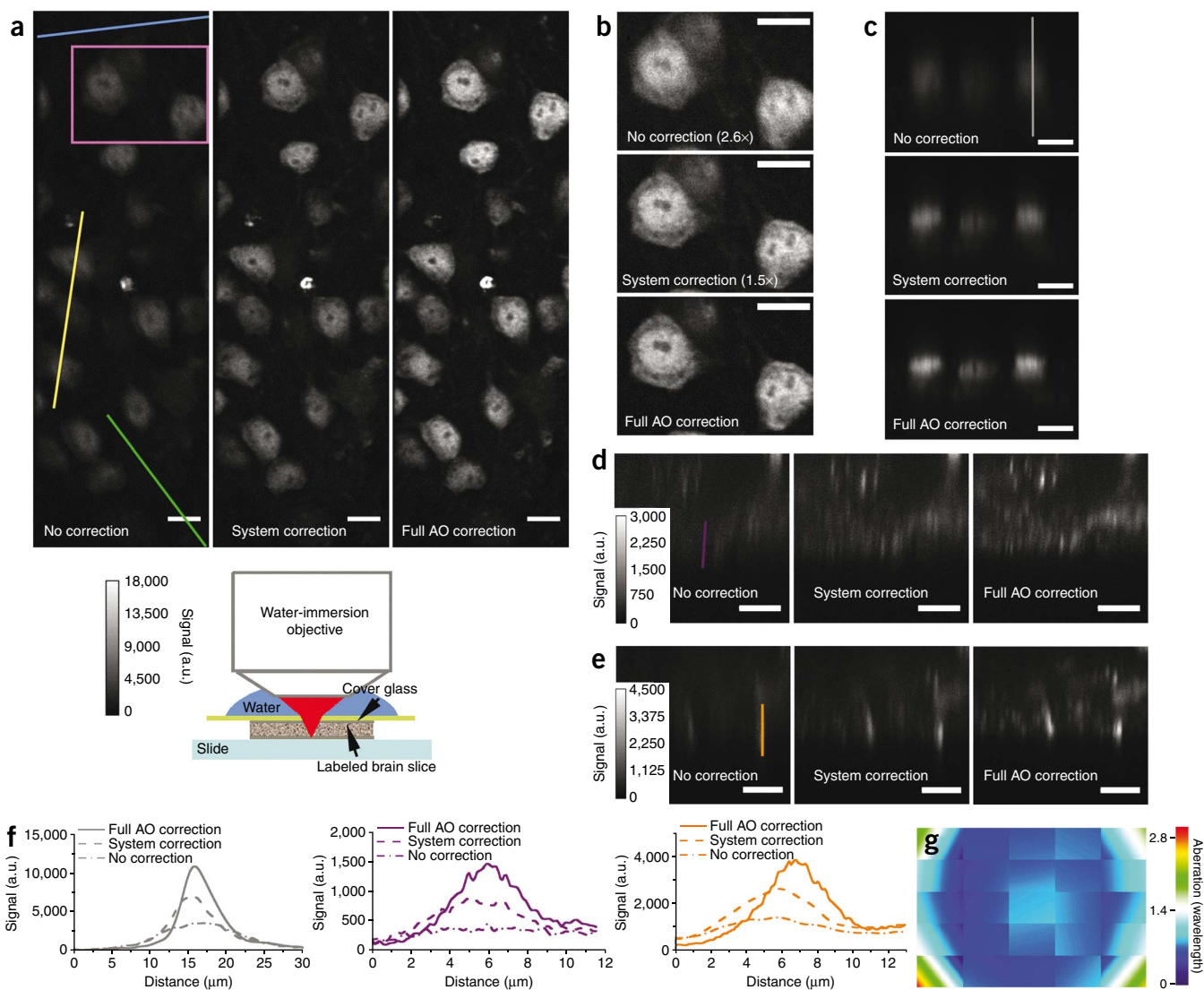


Figure 5 | Aberration correction at the bottom of an antibody-labeled 300- μm -thick fixed mouse brain slice with beam deflections measured by image correlation. **(a,b)** Experiment schematic is shown below **a**. Lateral images of a field of neurons acquired with and without correction as indicated **(a)**, and magnified images from one subfield marked by the rectangle in **a**, with all images normalized to the same peak intensity **(b)**. (See signal scale bar below **a**.) **(c–e)** Images in the axial planes defined by the yellow **(c)**, green **(d)** and blue **(e)** lines in **a**. Display gain was increased in **d** and **e** as indicated to highlight dendritic processes. **(f)** Intensity profiles along the gray, purple and orange lines in **c–e**. **(g)** The final corrective wavefront in units of excitation light wavelength (850 nm), after subtraction of system aberrations, for 36 subregions and direct phase measurement. Scale bars, 10 μm .

examples with measured or reconstructed phase illustrated that the phase measurement provides substantially greater improvement in resolution and signal than phase reconstruction because the measurement interval in this case is too coarse compared to the scale of the actual phase variation, leading to inaccurate reconstruction. However, when each mask was stepped in a 2×2 pattern of one-half the mask width both horizontally and vertically, the resulting fourfold greater measurement density led to a reconstruction yielding a comparable image improvement to that obtained by the independent algorithm with measured phase. If we used a 3×3 stepped pattern, the reconstruction provided an even more detailed map of the aberrated wavefront as well as the recovery of a near-diffraction-limited focus. We confirmed these trends for 25 simulated wavefronts (one of which is shown in **Supplementary Fig. 3**).

As all of the above examples used a small bead as a reference object for AO correction, it was straightforward to use the centroid

of the bead image to determine the beam deflections. However, the centroid approach can also be applied to any isolated punctate object native to the specimen. For example, we illustrate AO correction of a $\sim 20\text{-}\mu\text{m}$ -diameter pollen grain under a stack of four aberration-producing cover glasses, based on measuring the centroid of the grain itself (**Supplementary Fig. 9**). Of course, many samples will have more complicated morphologies for which a centroid is inaccurate or ill-defined. In these cases, image correlation can be used to measure the image shift when different pupil segments are turned on. For example, we corrected microscope system aberration using image correlation on an entire field of beads (**Supplementary Fig. 10**). The improvements in signal and resolution were similar to system correction by centroid measurement (**Supplementary Fig. 4**), as expected.

Image correlation also allowed us to apply our AO algorithm in complex biological tissues with arbitrary fluorescence patterns.

We antibody-stained the neurons near the top and bottom surfaces of a 300- μm -thick fixed brain slice for NeuN, a neuron-specific nuclear protein, using DyLight 594 as a fluorescent marker. We collected images of the top surface with no wavefront correction, after correction for only the system aberration and after full AO correction (**Supplementary Fig. 11**). We collected similar images of the bottom surface (**Fig. 5**). A cover slip placed over the slice contributed spherical aberration at both surfaces, and at the bottom surface, additional aberrations were introduced by the slice itself. We observed clear progression in signal and resolution as more aberrations were corrected (**Fig. 5a**). The improvement in image quality was even more apparent when we normalized no-correction, system-correction and full-correction images from a selected region to their respective peak signals (**Fig. 5b**). We observed a similar progression of resolution improvement in axial planes for both cell bodies (**Fig. 5c**) and finer dendritic structures (**Fig. 5d,e**).

We corrected the images in **Figure 5** using the independent mask algorithm with 5×5 subregions and direct phase measurement. However, AO correction using stepped overlap (4×4 with 2×2 steps) with phase reconstruction and image correlation on a slice of similar thickness can yield similar improvements in signal and resolution (**Supplementary Fig. 12**). These latter methods can also be used to improve signal and resolution in cortical brain slices from transgenic *thy1-GFP* line M mice (**Supplementary Fig. 13**). A survey of nine neurons and their corresponding corrective wavefronts at depths from 250 μm to 400 μm shows a common component owing to coverslip-induced spherical aberration but also distinct aberrations reflecting the unique refractive index inhomogeneities in the vicinity of each neuron.

One advantage of using image correlation for the beam-deflection measurements is that it measures the mean aberration over the entire user-selected correlation region and hence provides AO correction valid over that entire region. Thus, in the AO correction for 300 μm brain slice (**Fig. 5**), the signal and resolution were improved throughout the $46 \times 140 \mu\text{m}$ imaging area despite the fact that we used only a single corrective wavefront pattern (**Fig. 5g**). The corresponding disadvantage is that, because the measured aberration represents an average of the optical properties over a larger volume of biological tissue (**Supplementary Fig. 14**), correction of this averaged aberration will lead to less than optimal correction in specific subregions in which the local refractive index profile differs from the measured average. In such regions, more local measurements may be called for, using either local image correlation or centroid estimation of local features. The larger image would then be stitched together from smaller sub-images, each produced with a unique corrective wavefront.

The ability to distinguish more and finer dendritic structures in the neuropil with full AO correction (**Fig. 5d,e**) is particularly noteworthy. Coupled with the ability to provide useful correction over large areas (**Fig. 5a**) these observations suggest that AO might be fruitfully combined with *in vivo* calcium imaging of neural activity: a large field of view is needed to monitor multiple neurons simultaneously, and higher signal and tighter axial confinement of the excitation should lead to larger activity-modulated fluorescence changes in neurons, as well as reduced activity-insensitive background from the surrounding neuropil.

DISCUSSION

The principles of using pupil segmentation to measure beam deflection by image shift, for correction of aberrations in optical microscopy, that we described here may be applied to other point-scanning and widefield microscopes: far-field super-resolution techniques¹, for example, are exquisitely sensitive to aberrations (for example, see **Supplementary Fig. 15** for the AO correction of system aberration during the generation of an annular mode such as is used in stimulated emission depletion microscopy). Furthermore, application of our approach to confocal microscopy would be simplified by the linear rather than quadratic dependence of signal on intensity characteristic of two-photon microscopy.

The advantages of image-based AO methods such as ours that directly measure aberrations without a wavefront sensor over those relying on search algorithms has been discussed elsewhere⁸, with the important differences being the rate of convergence and the ability to reach a deterministic, diffraction-limited solution. Among these image-based methods, the elegant modal approaches^{21–27} stand out. Based on serially applying bias aberration modes described by Zernike^{21–25} or Lukosz^{26,27} functions, they derive the coefficients for each pupil-spanning mode from how it modulates the image intensity²⁵, focal radius²⁶ or spatial frequency content²⁷. In contrast, our approach, in the parlance of astronomical and ophthalmological AO, is a zonal one: the wavefront is measured and corrected in discrete zones that tile the entrance pupil of the imaging element. In these disciplines, zonal correction is generally preferred^{7,19,28}, owing to the difficulty of expressing complex wavefronts without resorting to a large number of high-order modes (**Supplementary Fig. 3**) as well as the difficulty of either measuring or generating modes beyond fourth²⁸ to sixth¹⁷ order. Certainly, the wavefronts we measured on cortical slices suggest that complexity is also common (but not universal; **Supplementary Fig. 16**) when imaging in brain tissue, a result in agreement with previous scanning interferometric measurements through a variety of biological specimens^{4,5}. Furthermore, the simulations comparing modal and zonal approaches (**Supplementary Fig. 3**) indicate that, even assuming ideal measurement and correction at all orders, approximately twice as many images are needed to achieve the same root mean square wavefront error by modal means as by our independent subregion algorithm with phase reconstruction. In addition, the tilt corrections for all subregions can be determined from only a single tiled image in which all subregions are turned on simultaneously but with different initial tilt offsets applied to each to spatially separate the multiple sub-images thus produced (**Supplementary Fig. 17** and Online Methods). An added advantage of our approach is that accurate centroid measurement of a micrometer-scale object typically requires only a few hundred photons²⁹. Beam displacement measurement and phase reconstruction are also insensitive to photobleaching occurring during the measurement process, unlike other imaged-based, intensity-dependent AO methods.

METHODS

Methods and any associated references are available in the online version of the paper at <http://www.nature.com/naturemethods/>.

Note: Supplementary information is available on the Nature Methods website.

ACKNOWLEDGMENTS

We thank our colleagues at Janelia Farm Research Campus, Howard Hughes Medical Institute, B. Shields, A. Hu, W. Amir, R. Kerr, J. Truman, M. Hooks and J. Makara for help with sample preparation, J. Osborne and S. Bassin for help with machining and T. Sato and T. Planchon for helpful discussions.

AUTHOR CONTRIBUTIONS

N.J. and E.B. designed the project; N.J., D.E.M. and E.B. developed the instrument control program; N.J. performed the experiments; and N.J. and E.B. wrote the paper.

COMPETING INTERESTS STATEMENT

The authors declare no competing financial interests.

Published online at <http://www.nature.com/naturemethods/>.

Reprints and permissions information is available online at <http://npg.nature.com/reprintsandpermissions/>.

- Ji, N. *et al.* Advances in the speed and resolution of light microscopy. *Curr. Opin. Neurobiol.* **18**, 605–616 (2008).
- Gibson, S.F. & Lanni, F. Experimental test of an analytical model of aberration in an oil-immersion objective lens used in three-dimensional light microscopy. *J. Opt. Soc. Am. A* **8**, 1601–1613 (1991).
- Kam, Z. *et al.* Computational adaptive optics for live three-dimensional biological imaging. *Proc. Natl. Acad. Sci. USA* **98**, 3790–3795 (2001).
- Schwertner, M. *et al.* Measurement of specimen-induced aberrations of biological samples using phase stepping interferometry. *J. Microsc.* **213**, 11–19 (2004).
- Schwertner, M., Booth, M.J. & Wilson, T. Characterizing specimen induced aberrations for high NA adaptive optical microscopy. *Opt. Express* **12**, 6540–6552 (2004).
- Babcock, H.W. Adaptive optics revisited. *Science* **249**, 253–257 (1990).
- Tyson, R.K. *Principles of adaptive optics* (Academic Press, Inc., San Diego, 1991).
- Booth, M.J. Adaptive optics in microscopy. *Philos. Transact. A Math. Phys. Eng. Sci.* **365**, 2829–2843 (2007).
- Liang, J., Williams, D.R. & Miller, D.T. Supernormal vision and high-resolution retinal imaging through adaptive optics. *J. Opt. Soc. Am. A Opt. Image Sci. Vis.* **14**, 2884–2892 (1997).
- Rueckel, M., Mack-Bucher, J.A. & Denk, W. Adaptive wavefront correction in two-photon microscopy using coherence-gated wavefront sensing. *Proc. Natl. Acad. Sci. USA* **103**, 17137–17142 (2006).
- Artal, P. *et al.* Odd aberrations and double-pass measurements of retinal image quality. *J. Opt. Soc. Am. A Opt. Image Sci. Vis.* **12**, 195–201 (1995).
- Porter, J. *et al.* eds. *Adaptive optics for vision science* (John Wiley & Sons, Inc., Hoboken, New Jersey, USA, 2006).
- Born, M. & Wolf, E. *Principles of Optics* (Cambridge University Press, Cambridge, England, 1999).
- Goodman, J.W. *Introduction to Fourier optics* 3rd ed. (Roberts & Company Publishers, Englewood, Colorado, USA, 2005).
- Richards, B. & Wolf, E. Electromagnetic diffraction in optical systems. II. structure of the image field in an aplanatic system. *Proc. R. Soc. Lond. A Math. Phys. Sci.* **253**, 358–379 (1959).
- Wang, J.Y. & Silva, D.E. Wave-front interpretation with Zernike polynomials. *Appl. Opt.* **19**, 1510–1518 (1980).
- Fernandez, E.J. *et al.* Adaptive optics with a magnetic deformable mirror: applications in the human eye. *Opt. Express* **14**, 8900–8917 (2006).
- Devaney, N. *et al.* Characterisation of MEMs mirrors for use in atmospheric and ocular wavefront correction. *Proc. SPIE* **6888**, 688802 (2008).
- Panagopoulou, S.I. & Neal, D.R. Zonal matrix iterative method for wavefront reconstruction from gradient measurements. *J. Refract. Surg.* **21**, S563–S569 (2005).
- Southwell, W.H. Wave-front estimation from wave-front slope measurements. *J. Opt. Soc. Am.* **70**, 998–1006 (1980).
- Neil, M.A.A. *et al.* Adaptive aberration correction in a two-photon microscope. *J. Microsc.* **200**, 105–108 (2000).
- Booth, M.J. *et al.* Adaptive aberration correction in a confocal microscope. *Proc. Natl. Acad. Sci. USA* **99**, 5788–5792 (2002).
- Booth, M.J., Neil, M.A.A. & Wilson, T. New modal wave-front sensor: application to adaptive confocal fluorescence microscopy and two-photon excitation fluorescence microscopy. *J. Opt. Soc. Am. A Opt. Image Sci. Vis.* **19**, 2112–2120 (2002).
- Débarre, D. *et al.* Adaptive optics for structured illumination microscopy. *Opt. Express* **16**, 9290–9305 (2008).
- Débarre, D. *et al.* Image-based adaptive optics for two-photon microscopy. *Opt. Lett.* **34**, 2495–2497 (2009).
- Booth, M.J. Wavefront sensorless adaptive optics for large aberrations. *Opt. Lett.* **32**, 5–7 (2007).
- Debarre, D., Booth, M.J. & Wilson, T. Image based adaptive optics through optimisation of low spatial frequencies. *Opt. Express* **15**, 8176–8190 (2007).
- Hardy, J.W. *Adaptive Optics for Astronomical Telescopes* (Oxford University Press, Oxford, UK, 1998).
- Thompson, R.E., Larson, D.R. & Webb, W.W. Precise nanometer localization analysis for individual fluorescent probes. *Biophys. J.* **82**, 2775–2783 (2002).

ONLINE METHODS

Animal use. All experiments were performed according to methods approved by the Janelia Farm Institutional Animal Care and Use Committee.

AO two-photon fluorescence microscope. A simplified schematic of our microscope is given in **Supplementary Figure 1a**. A near-infrared light beam from a femtosecond pulsed titanium:sapphire (Ti:Sa) laser (Chameleon Ultra II; Coherent Inc.) is reflected from a pair of galvanometers (X and Y, 3-mm beam aperture; model 6215H; Cambridge Technology Inc.) for eventual two-dimensional raster scanning. The galvanometers are made optically conjugate to one another with two custom-made 30 mm focal-length telecentric f - θ (F1) lenses (Special Optics). A third F1 lens and a custom-made 150-mm focal-length telecentric f - θ (F5) lens (Special Optics) serve to conjugate the Y galvanometer to a liquid-crystal phase-only spatial light modulator (SLM) ($1,920 \times 1,080$ pixels; PLUTO-NIR; Holoeye Photonics AG) and also expand the beam $5\times$ to better match the 15.4×8.6 mm dimensions of the SLM. Conjugation of the galvanometers to the SLM insures that the intensity at each subregion of the SLM remains constant, even during beam scanning. Depending on the objective used, the SLM is itself either conjugated by a pair of F5 lenses to the 16-mm-diameter rear pupil of a $20\times$, NA 1.0 water-dipping objective (W Plan-Apochromat; Carl Zeiss Inc.), or by the combination of a custom-made 120-mm focal-length telecentric f - θ (F4) lens (Special Optics) and a custom-made 240-mm focal-length telecentric f - θ (F8) lens (Special Optics) to the 20-mm-diameter rear pupil of a $16\times$, NA 0.8 water-dipping objective (model LWD $16\times$ W; Nikon Corp.). Conjugation of the SLM to objective rear pupil here is critical, particularly for aberrations of rapidly varying phase, or else the corrective phase pattern applied at the SLM would move across the rear pupil during scanning, resulting in an improper correction over much of the field of view. A field stop located at the intermediate image plane between the F5 lenses serves to block light from undesirable higher diffraction orders, specular reflection from the front surface of the SLM and light intentionally diffracted from 'off' subregions. For the Zeiss objective (design NA 1.0), the $1/e^2$ beam radius σ is 6.0 mm at both the SLM and the rear pupil, for a fill factor $\sigma/a = 0.75$ normalized to the rear pupil radius a . For the Nikon objective (design NA 0.8), the $1/e^2$ beam radius σ is 6.0 mm at the SLM and 12.0 mm at the rear pupil, for a normalized fill factor $\sigma/a = 1.2$. These fill factors insure that effective phase corrections can be applied over most of the beam and that most of the beam energy enters the objective. The lower fill factor of the Zeiss objective makes the objective better suited for *in vivo* imaging at depth³⁰, whereas the higher fill in the Nikon objective more effectively uses the objective NA to maximize resolution. For the Zeiss objective, the SLM area used in AO correction is rectangular, whereas for the Nikon objective, the SLM area is square. The dimensions of the SLM relative to the back aperture of the Zeiss and Nikon objectives are shown in **Supplementary Figure 18**. In the detection path, a dichroic long-pass beamsplitter (TPE BS; model FF665-Di02-25x36; Semrock) immediately above the objective transmits the excitation light and reflects the fluorescence signal, which is then detected at photomultiplier tubes (PMT; model H7422-40, Hamamatsu). Ray-tracing software, Oslo (Sinclair Optics, Inc.) and Zemax

(Zemax Development Corp.) was used to design the custom f - θ lenses and simulate the microscope performance along the entire optical path.

A detailed schematic of our microscope is presented in **Supplementary Figure 1b**. An electro-optic modulator (model 350-80LA; Conoptics Inc.) combined with a beam pickoff (model 7940; Omega Optical), a photodetector (model PDA100A; ThorLabs) and a proportional-integral-differential controller (model SIM960; Stanford Research Systems; not shown in **Supplementary Fig. 1b**) in an analog feedback loop was used to: (i) set the desired laser intensity at the sample; (ii) stabilize the laser intensity; and (iii) blank the beam, when not scanning, or during x galvanometer fly-back, while scanning. A filter wheel (Lambda 10-B; Sutter Instruments) with a series of neutral density filters further extends the dynamic range over which the power can be reliably controlled (0.01–100%). A $2\times$ beam expander (model BE02M-B; Thorlabs Inc.) minimizes divergence of the beam over the long path from the electro-optic modulator to the microscope. Conversely, a $2\times$ beam reducer (model BE02M-B; Thorlabs Inc.) mounted on a fast translation stage (model M-663; Physik Instrumente, GmbH) can be shuttled into the path of the beam immediately before the microscope to concentrate the beam onto a subsection of the SLM, when needed. A pair of mirrors mounted on an identical pair of fast translation stages then position the beam in two dimensions relative to the SLM. The operation of the beam reducer and the laser positioning mirrors is explained below.

The microscope objective is mounted to a fast single axis piezoflexure stage (model P-733.ZCL; Physik Instrumente, GmbH) for two- and three-dimensional imaging in the axial direction. Along the detection path, fluorescence is first collimated by one lens (L1) (model LA1002-A; Thorlabs), split into red and green components by a custom dichroic beamsplitter (model Q560DCXR; Chroma Technology Corp.), refocused by two additional lenses (L2 and L3) (Thorlabs) and then detected at the two PMTs. Green fluorescence is selected at the first PMT with a pair of filters (FL1) (glass filter (model CG-BG-39-1.00-2; CVI) and bandpass (model FF01-510/84; Semrock)), and red fluorescence is selected at the second PMT with a different filter pair (FL2) bandpass (model FF01-617/73; Semrock) and bandpass (model FF01-630/69; Semrock). Low noise current amplifiers (model DLPCA-200; FEMTO Messtechnik, GmbH) boost the signals measured at the two PMTs, and fast-resetting custom analog integrators are used to sum the resulting amplified current spikes over the time course of each pixel, yielding two final signals that are digitized to form red and green images.

Operation of the phase-only SLM. The phase-only SLM is used to both measure and then correct any aberrations. The SLM is divided into subregions. Specific subregions are turned 'off' (meaning that the light that is impinging on them does not reach the objective) by applying a phase grating consisting of alternate rows of 0 and π phase shift. This diffracts most of the light from these subregions to a field stop at an intermediate image plane, where it is blocked. In the 'on' subregions, a gentler, global phase ramp is applied to separate the large fraction of light modulated in the SLM from the small fraction of light specularly reflected from the front surface, which cannot be controlled. The global ramp is chosen to provide a nominal separation of 20–50 μm between the

modulated and specularly reflected beams at the sample, although usually the field stop is positioned to block the latter. The gradient in gray levels per pixel that must be programmed into the SLM to affect a given beam displacement at the image plane depends on the wavelength, the magnification ratio between SLM and objective rear pupil, the focal length of objective and other factors. For the Nikon objective configuration and $\lambda = 850$ nm, a global ramp of 3.139 gray levels per pixel at the SLM yields a 10 μm shift in image plane. After AO correction, different phase ramps and phase offsets unique to each subregion are superimposed upon the global phase ramp to produce the necessary correction based on the beam deflections and measured or reconstructed phases determined during execution of the AO algorithm. The relationship between the 8-bit gray level used to control the SLM and the actual phase shift produced was determined by calibration according to the manufacturer's recommendations.

Details of the pupil segmentation-based AO algorithm. First, the image plane chosen for AO correction is selected by acquiring a three-dimensional stack of images of a feature of interest, such as a fluorescent reference bead, and selecting the plane in which the signal is maximal, as integrated over a user-defined region of interest. Presumably, this plane is closest to the original ideal focus and hence will require the least correction to recover diffraction limited performance. For beam deflection measurements with N subregions, the power is initially increased at least N -fold, to compensate for the fact that only one subregion is 'on' at a time. Additional power adjustments are automatically made at each subregion as needed to yield enough signal to measure the image displacement accurately but not so much as to cause excessive photobleaching.

We used two different approaches for direct phase measurement. In the first, the phase in each subregion is adjusted to interfere with a central reference subregion. In the second, each subregion is interfered with all other subregions. In both cases, power is again adjusted as needed to achieve sufficient signal, but no more. To further minimize bleaching, only 5 images are acquired at equally spaced phase offsets between 0 and 2π for each subregion: the exact phase offset, ϕ_o , for maximum constructive interference is determined by fitting the signal at the focus from each of these images to the function $|1 - S| = |1 + \alpha \exp(i(\phi - \phi_o))|^4$, in which S represents the two-photon signal arising from the interference of the electric field from the current subregion with that from either the reference subregion or all other subregions. A background image with all subregions 'off' is acquired whenever the power level is changed, and subtracted from all subsequent images acquired at the same power level, to insure the accuracy of the measurements.

For the majority of the images acquired in this work, ~ 1 – 3 mW of power at $\lambda = 850$ nm was delivered through the objective, when all subregions were on. However, during beam deflection measurements in single subregions, ~ 10 – 30 mW might be used to generate sufficient signal at the much lower effective numerical aperture then prevailing. Typical imaging speeds during the algorithm were 50–100 pixels ms^{-1} . The SLM frame rate was 60 Hz, and we waited five frames for each new SLM pattern to stabilize. Additional time was required to center the input beam at the current 'on' subregion, as needed. Applying these numbers to the beam deflection, phase and background measurements and

adding further computational overhead, we find empirically that ~ 6 s is required to determine and then apply the appropriate corrective pattern in each subregion, when phases are measured directly. When the phase is reconstructed algorithmically from the deflection measurements alone, this time was reduced to ~ 1 s. We expect additional improvements with more efficient coding.

After the AO algorithm is complete, the pattern on the SLM represents the final corrective wavefront, modulo 2π . To display this wavefront in a more intuitive form, the global phase ramp used during measurement is subtracted, and the phase is unwrapped by counting fringes and assuming that the phase is continuous across subregion boundaries. Finally, to determine the aberration resulting from the sample alone, the portion of the unwrapped wavefront resulting from system aberrations is subtracted.

Adaptive optical correction for system aberration. Aberrations affecting the performance of a microscope can come from anywhere along the optical path from the source to the focus, as well as from the sample itself. It is therefore necessary to characterize these intrinsic microscope aberrations to be able to derive sample-induced aberration in subsequent experiments. Images were acquired of a 500-nm-diameter fluorescent bead through the Zeiss objective under the water immersion conditions for which the objective was designed (**Supplementary Fig. 4**). Marked astigmatism and coma were observed (**Supplementary Fig. 4a,c,e**), largely attributable to poor flatness of the SLM. However, after applying our AO algorithm with 36 independent subregions and direct phase measurement, the full width at half maxima of the bead images in both the lateral (**Supplementary Fig. 4a,b,g**) and axial (**Supplementary Fig. 4c–f,h**) directions approached their diffraction-limited values. The final corrective wavefront for system aberration, (**Supplementary Figs. 4i**) has a peak-to-valley variation of $\sim 1.7\lambda$, consistent with the typical flatness of SLM panels. Similar results were obtained when this same correction was applied to a field of beads over a $\sim 13 \times 13 \mu\text{m}$ field of view, indicating that the system correction is field independent (**Supplementary Fig. 5** and **Supplementary Movie 2**).

Different mask approaches to map the rear pupil. We explored several different approaches to segmenting the rear pupil for AO correction (**Supplementary Fig. 8**). The first, the independent mask approach (for example, **Supplementary Fig. 8a,b**), segmented the pupil into non-overlapping areas. Each area, or 'mask', is turned 'on' individually during the beam deflection measurements. The number of pupil subregions is equal to the ratio of the pupil area to the mask area, and the corrective wavefront in each masked region is estimated by a plane independent from that in all other regions.

In the overlapping mask approach (for example, **Supplementary Fig. 8c,d**), every mask that is individually 'on' during beam deflection measurement overlaps with other masks. As a result, the total number of planar subregions in the final corrective wavefront is larger than the ratio of the pupil area to the mask area. However, the final values of phase in these subregions may not be fully independent from one another, owing to mask overlap.

Finally, in the stepped overlapping mask approach, every mask has the same dimensions but is displaced from its neighbors by a distance less than the dimension of the mask. For example, the pattern described in **Supplementary Figure 8d** is denoted 3×3

with 2×1 stepped overlapping masks: ' 3×3 ' denotes the dimension of each mask (three horizontal \times three vertical masks to span the rear pupil), and ' 2×1 ' denotes the stepping pattern (two steps to cross the width of each mask and one step to cover the height). This approach particularly well suited to phase reconstruction, as it permits a dense array of phase gradient data to be measured on a regular interval.

Choosing the number of pupil segments. The simulations shown in **Supplementary Figure 3** give an indication how rapidly a corrective wavefront can converge to the desired solution for both the modal approach and the several variations of our pupil segmentation approach described above. Note that, despite the comparatively^{4,5} mild spatial frequency content in the simulated wavefront, modal correction through fourth order (typical of that applied experimentally^{24–26}) is inadequate to accurately reproduce the fine phase structure, whereas subregion sampling, typical of that used here, yields a much more accurate estimation.

Experimentally, the images in **Supplementary Figure 7** demonstrate, for the case of a 250- μm -thick slice of fixed cortical tissue, how the lateral resolution, axial resolution and signal each vary as a function of N , for the independent algorithm and direct phase measurement. Little improvement in lateral resolution is seen for any N value, a result consistent with previous calculations of the effects of aberration on resolution³¹. However, even with only 12 subregions, both the signal and the axial resolution improved significantly. With increasing N thereafter, the improvement in axial resolution rapidly reached saturation, perhaps indicating that even with modest N values, most rays intersect near a common point, so the region of marked two-photon fluorescence generation is largely confined to a near-diffraction limited volume. The signal, however, continued to increase until $N = 25$, indicating greater sensitivity of the two-photon signal to even small wavefront errors. This is also understandable: a phase error ϕ in the electric field over only a small fraction α of the rear pupil will yield a signal $|1 - \alpha(1 - \exp(i\phi))|^4$ less than optimal at a point object, for example, 41% of optimal even if only 10% of the wavefront in the rear pupil is 180° out of correct phase.

In short, the number of subregions required will depend on the specifics of the sample under investigation, the parameter being optimized and the extent of optimization desired. One additional advantage of our approach is that an initial low-resolution map of the aberrated wavefront can be made at modest N , and then only the areas suggestive of fine structure need be sampled with finer subregions.

AO correction with a single composite image. One advantage of using an SLM is that a different phase ramp can be applied to each subregion and, when combined with phase reconstruction, can be used to determine the entire requisite AO correction from a single composite image. These phase ramps split the excitation light from each subregion in a different direction, forming multiple foci within the sample (for example, nine foci in **Supplementary Fig. 17**). If there were no aberration, the images of a 1- μm bead

generated by these foci would fall on a 3×3 array with a 6.4 μm period imposed by the applied phase ramps (**Supplementary Fig. 17c**). The deviations of the various bead images from this ideal array (**Supplementary Fig. 17b**) indicate the degree of aberration (in this case, system aberration in the Nikon objective configuration), from which the aberration-induced beam deflection or, equivalently, the local slope of the aberration wavefront was determined at each of the nine subregions. The phase reconstruction algorithm was then used to obtain the final corrective wavefront (**Supplementary Fig. 17d**), which yielded a signal improvement similar to that obtained by the 3×3 independent mask algorithm with direct phase measurement (**Supplementary Fig. 17e**). Although this parallel approach to wavefront slope measurement is similar to that used in the Shack-Hartmann wavefront sensor, the principles by which the image arrays are generated are distinct.

Bead sample preparation. We immobilized 500-nm and 1- μm fluorescent beads (Fluosphere carboxylate-modified microsphere; Invitrogen Corp.) were immobilized on poly(L-lysine)-coated microscope slides (Superfrost; Fisher Scientific).

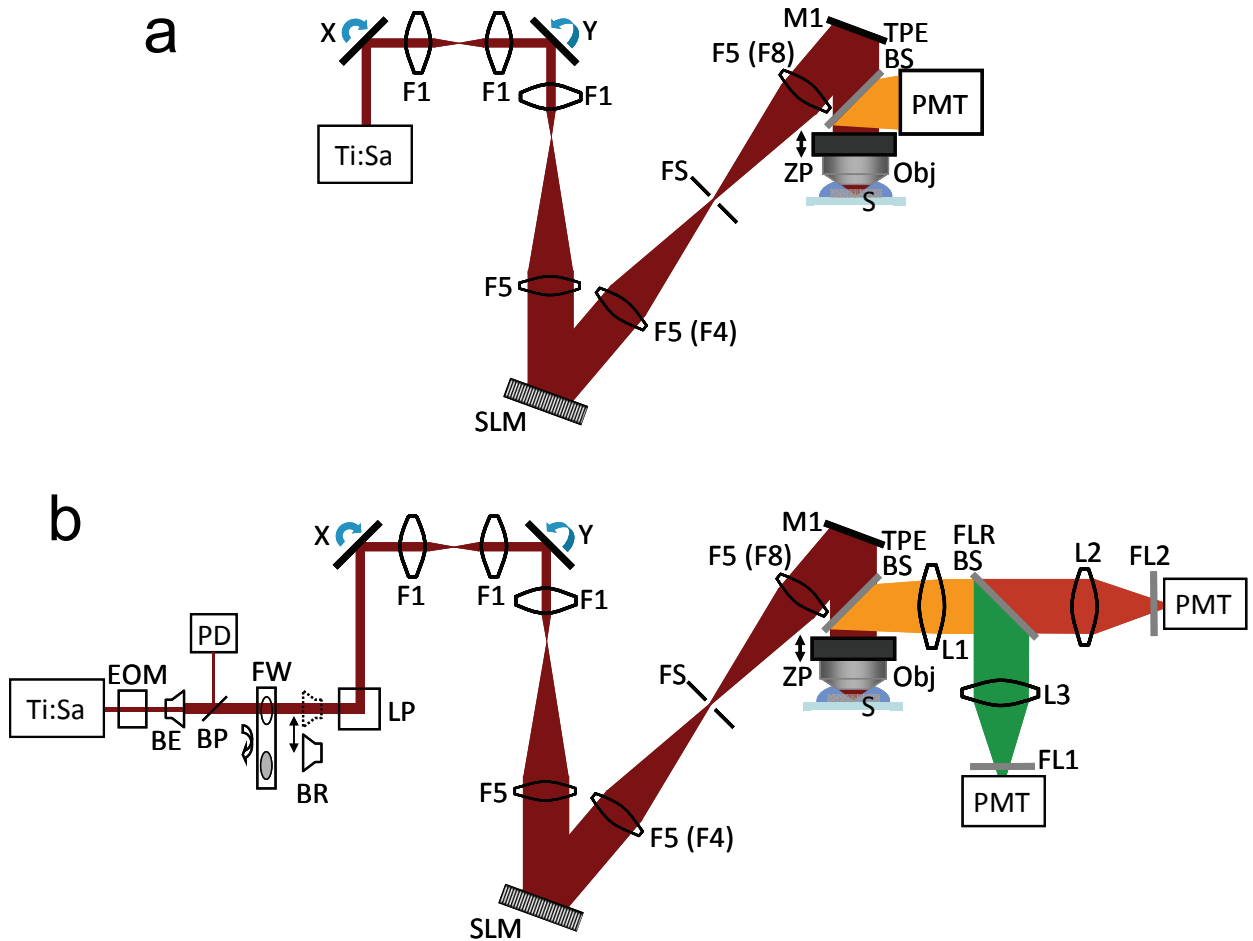
Pollen grain sample preparation. Three microscope cover glasses (Squares No. 1.5; Fisher Scientific) were stacked on top of a microscope slide containing fluorescent mixed pollen grains (Carolina Biological Supply Co.). Including the cover glass supplied with the slide, the excitation light traveled through four pieces of cover glasses before reaching the pollen grain.

Fixed brain slice preparation. Mice were fixed with 4% paraformaldehyde in 0.1 M phosphate buffer (PB) (pH 7.4) via transcardiac perfusion. The brains were post-fixed at 4°C overnight for about 20 h, then washed three times with PBS. After embedding in 5% agarose (Lonza Group Ltd.), sections were cut on a Leica VT1200S vibrating microtome, free-floated in PBS and stored at 4°C until use. For antibody labeling, selected sections were transferred to a 24-well dish with fresh PBS and washed briefly at room temperature (25°C). Sections were blocked with 5% normal goat serum (Vector Laboratories Inc.), 0.3% Triton X-100 (Acros Organics) in PBS for 2 h at room temperature, then incubated in mouse antibody to NeuN (MAB377; lot LV1427917; Chemicon, now Millipore Corp.) (1:600) diluted in block at 4°C overnight for about 25.5 h. The following day, the sections were washed three times for 20 min each in PBS, 0.1% Triton X-100, then incubated in goat anti-mouse DyLight 594 (115-515-003, lot 82339; Jackson ImmunoResearch Laboratories, Inc.) (1:400) diluted in block at room temperature for 2.5 h. Sections were washed three times for 5 min each in PBS, then mounted onto glass slides (Superfrost plus; Fisher Scientific) and embedded with Vectashield (Vector Laboratories Inc.) under coverslips. All incubations and washes were performed with gentle agitation.

30. Oheim, M. *et al.* Two-photon microscopy in brain tissue: parameters influencing the imaging depth. *J. Neurosci. Methods* **111**, 29–37 (2001).

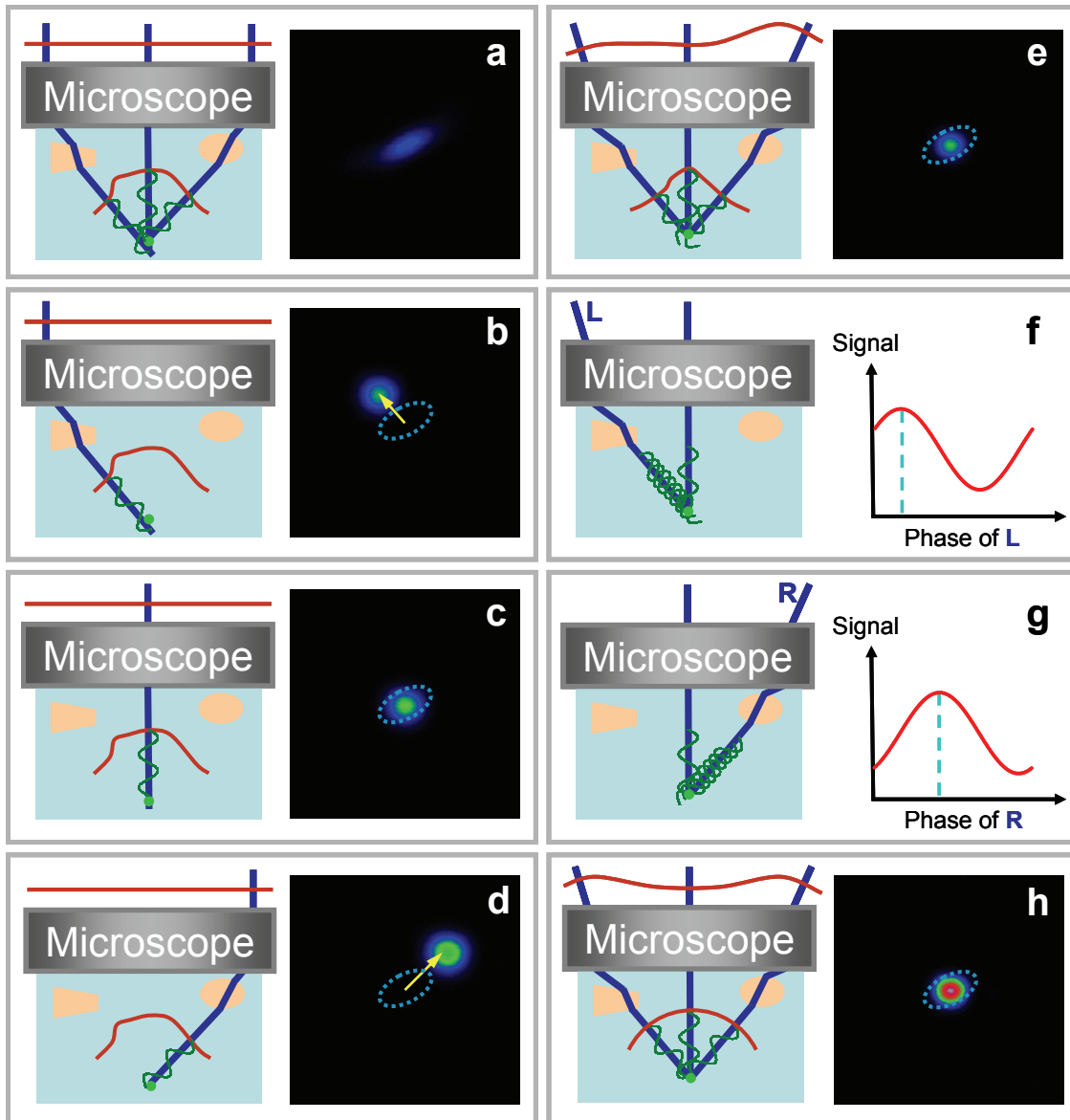
31. Sheppard, C.J.R. & Gu, M. Aberration compensation in confocal microscopy. *Appl. Opt.* **30**, 3563–3568 (1991).

Supplementary Figure 1 Simplified and detailed schematics for our adaptive-optical (AO) two-photon fluorescence microscope.



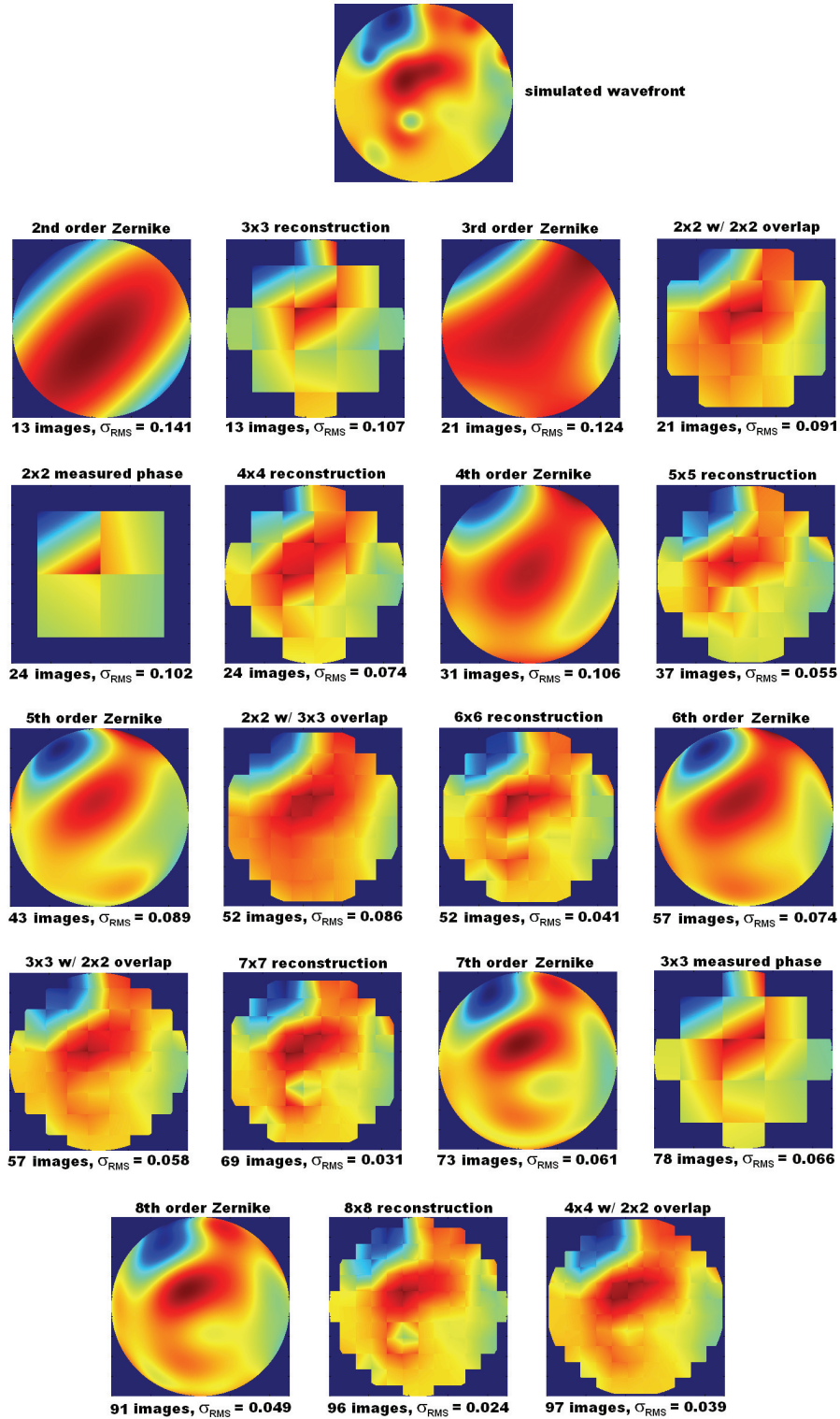
Supplementary Figure 1. (a) The essential components of our AO two-photon fluorescence microscope. (b) Detailed components of the microscope: Ti:Sapphire laser; electro-optical modulator (EOM); 2× beam expander (BE), beam pickoff (BP) that reflects ~3% of the light into a photodiode (PD); neutral-density filter wheel (FW); 2× beam reducer on motorized translation stage (BR); pair of mirrors mounted on independent motorized stages for two-axis laser positioning (LP); X galvanometer (X), two 30mm focal-length telecentric f-θ lenses (F1); Y galvanometer (Y); 30mm (F1) and 150mm (F5) focal-length telecentric f-θ lenses; spatial light modulator (SLM), pair of telecentric f-θ relay lenses (two 150mm focal-length lenses (F5) for Zeiss objective configuration, one 120mm (F4) and one 240mm (F8) lens for Nikon objective configuration); field stop (FS) at an intermediate image plane between them; protected-silver mirror (M1); dichroic long-pass beamsplitter (TPE BS) to separate excitation light from fluorescence; Zeiss or Nikon water dipping objective (Obj) mounted on a Z-piezo stage (ZP); sample (S); fluorescence collimating lens (L1); dichroic fluorescence beamsplitter (FLR BS) to separate green and red fluorescence; two lenses (L2, L3) to focus fluorescence through two filter sets (FL1, FL2) onto two photomultiplier tubes (PMT).

Supplementary Figure 2 Step-by-step description of our pupil-segmentation based AO algorithm.



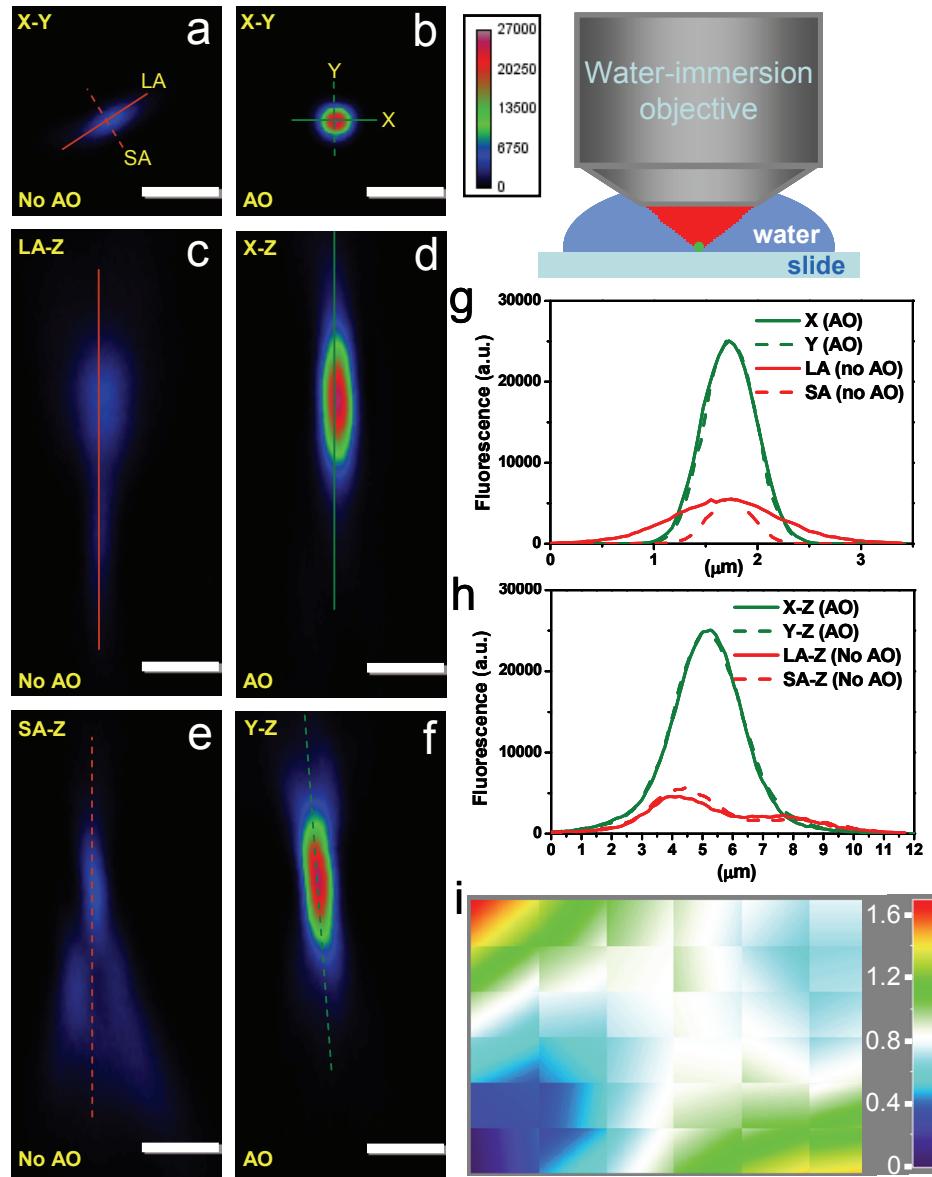
Supplementary Figure 2. Sketches illustrating our AO algorithm using three independent subregions, creating three beamlets (blue rays). (a) Aberrated wavefront (red) due to refractive index inhomogeneities (orange) leads to an aberrated image of a reference bead. (b,c,d) Images acquired with the left, center, and right subregions, respectively, permit the tilt of each beamlet to be measured from the displacement of the bead. (e) Beamlets intersect at a common point, after appropriate compensatory tilts are applied at the SLM. (f) Interference of left beamlet with central reference beamlet, at several phase offsets (green sinusoids) applied to the former, determines the optimal phase offset (dashed aqua line); (g) Same procedure applied to the right beamlet. (h) Final corrected wavefront (red) and recovered diffraction-limited focus. An example with actual data showing the images and SLM patterns during the AO correction with $N = 36$ subregions is given in **Supplementary Movie 1**. If phase reconstruction is used, the phase measurement steps (f and g) are skipped, and the optimal phase offset in each subregion is determined algorithmically.

Supplementary Figure 3 Simulations comparing modal and zonal representations of a complex aberration pattern, the latter obtained using different variants of our AO algorithm.



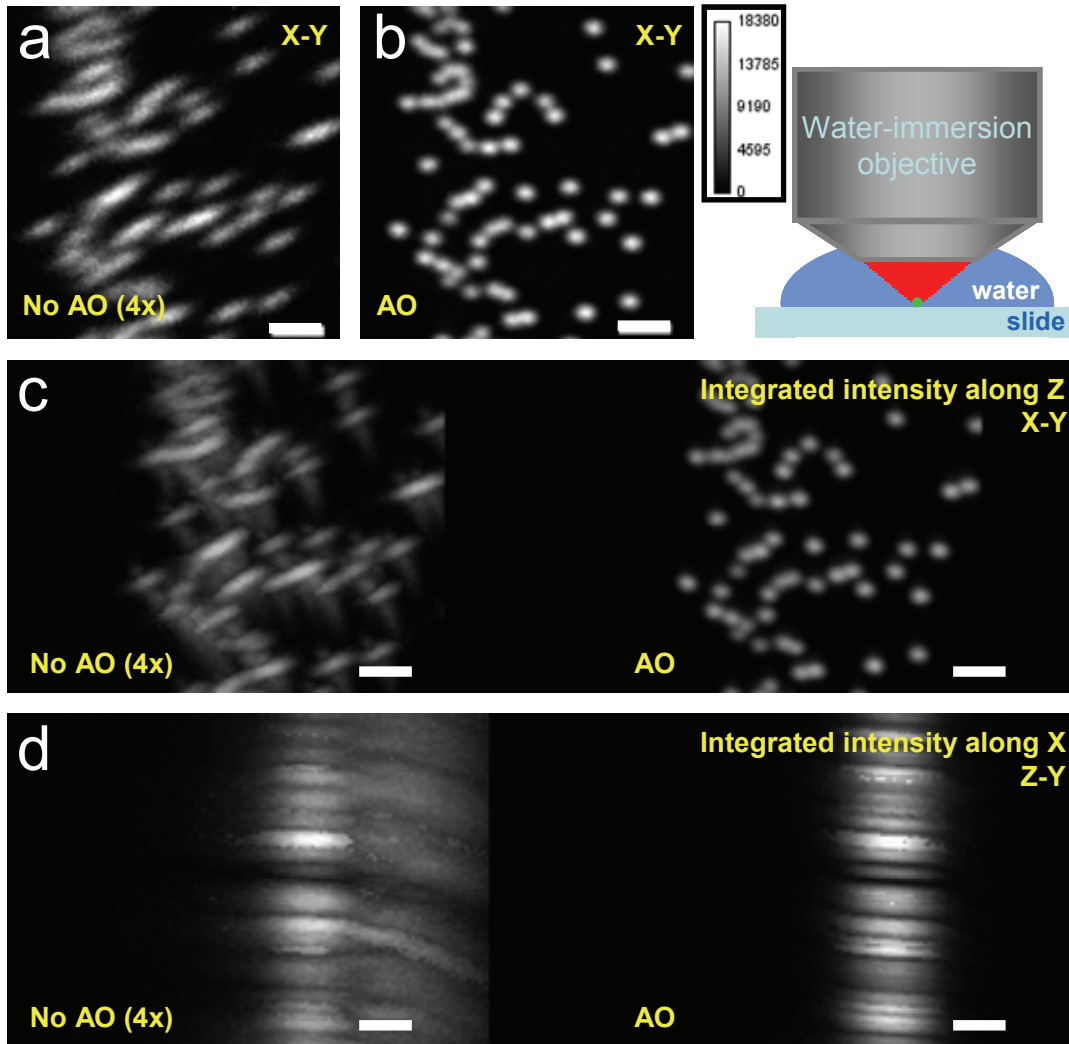
Supplementary Figure 3. Modal and zonal representations of a complex aberration pattern (top image). The representations are ordered by the number of images required for AO correction, using the method listed at the top of each. For modal representations (e.g., “ Z^{th} order Zernike”), $2N+1$ images are needed to correct for all N Zernike modes through order Z (Ref. 25). Zonal representations were estimated using different variants of our pupil segmentation algorithm (see Results). Measured phase requires $6N$ images for N subregions, assuming one for beam deflection measurement and five for phase. Phase reconstruction requires only N images for N beam deflection measurements. Higher density sampling is achieved with stepped overlap, but at the cost of more images. The root mean square error σ_{RMS} between each representation and the original simulated wavefront, normalized to the peak-to-peak amplitude of the latter, is listed for each scenario, and represents the average from 25 simulated wavefronts. For a similar number of images required, zonal representations of the wavefront obtained via phase reconstruction with either independent or stepped overlapping masks always describe complex aberration patterns more accurately than the modal representation.

Supplementary Figure 4 Correction of system aberration.



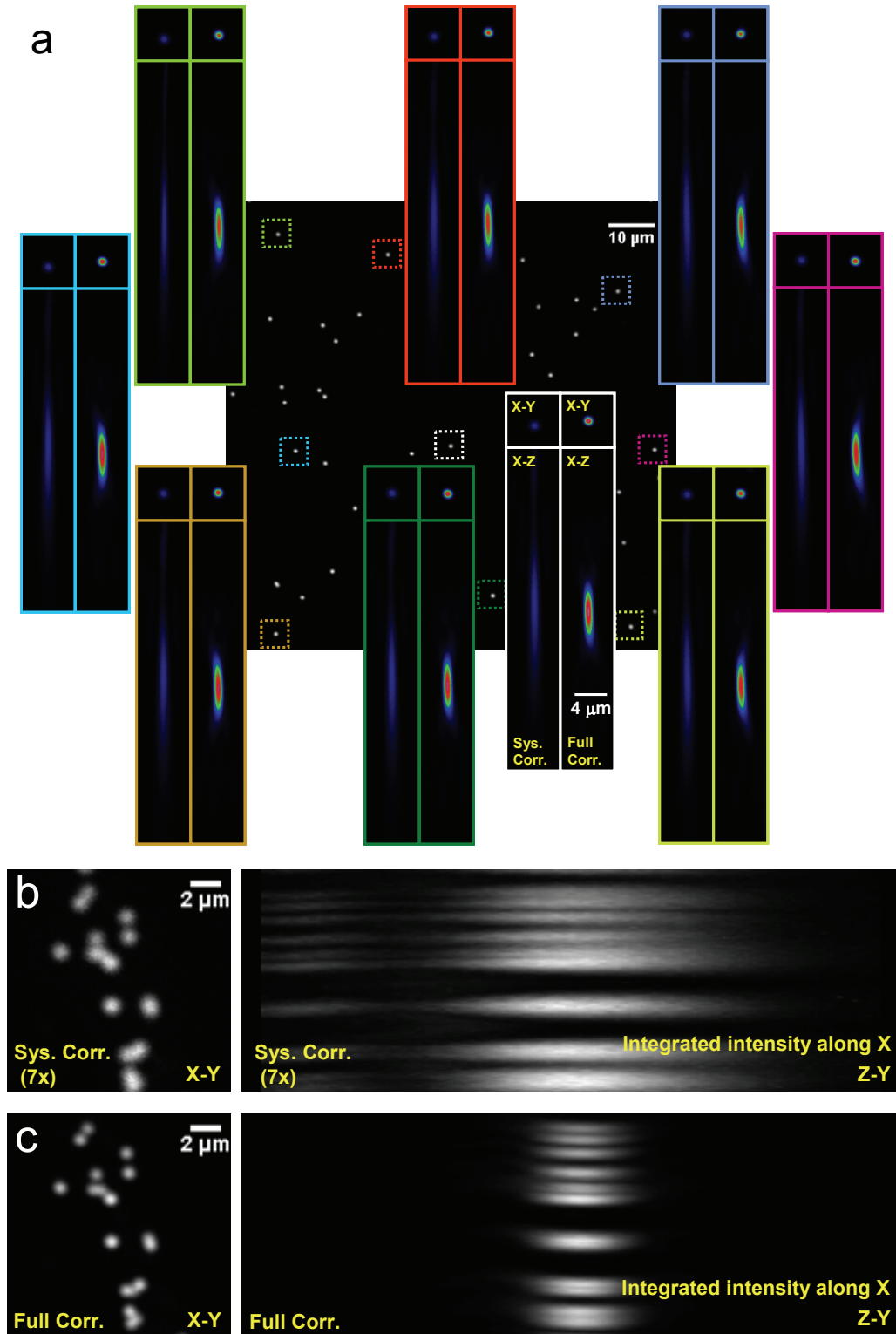
Supplementary Figure 4. Images of a 500 nm fluorescent bead immersed in the design medium of water (inset, upper right), both before (**a,c,e**) and after (**b,d,f**) AO correction with $N = 36$ independent subregions and measured phase (see Results). In both cases, three orthogonal image planes were selected: X–Y, and either LA–Z, SA–Z or X–Z, Y–Z, where Z denotes the axial direction, and LA and SA denote the long and short axes, respectively, of the bead image before correction. (**g**) Comparative intensity profiles along lines drawn in the X–Y lateral plane (red and green in **a,b**). (**h**) Similar profiles along lines drawn in the axial planes (red and green lines in **c,d,e,f**). (**i**) The final corrective wavefront for system aberrations in our microscope when using a Zeiss 20x, 1.0NA objective, in units of wavelength λ ($\lambda = 850\text{nm}$). Scale bar: 2 μm .

Supplementary Figure 5 Application of system correction obtained from one bead to a field of beads.



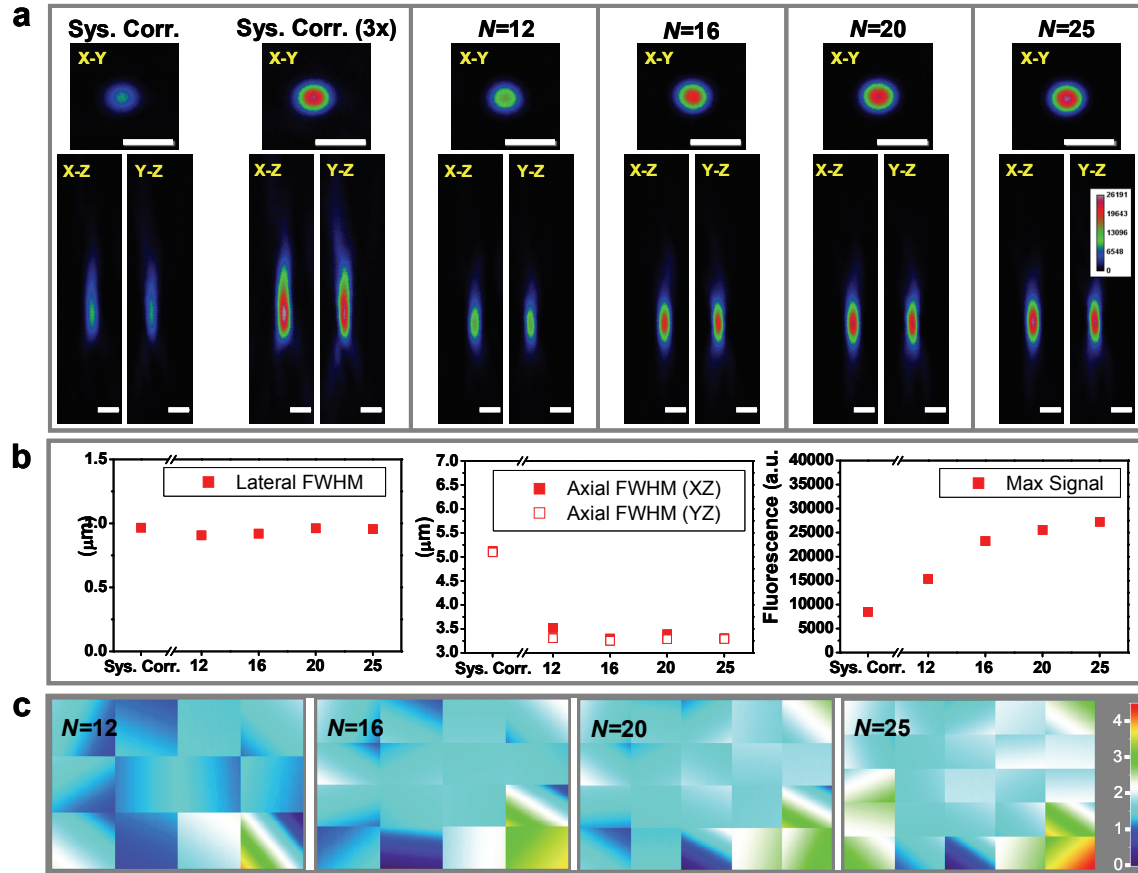
Supplementary Figure 5. Applicability of AO correction for system aberration at one point over a larger field of view. (a) Lateral image of a field of 500 nm diameter fluorescent beads before AO correction. (b) Image of the same beads, after applying the system correction determined from the central bead. (c) Lateral (X-Y) integrated intensity projection obtained by summing the entire 3D image stack along the axial Z direction. (d) Axial Z-Y intensity projection integrated along the lateral X direction. Display gain of the left, uncorrected images in a-c is increased 4× in (c,d) to improve visibility. Rotating integrated intensity projections distilled from the uncorrected and corrected 3D image stacks are shown in **Supplementary Movie 2**. Scale bar: 2 μm .

Supplementary Figure 6 Aberration correction for a field of beads in air observed with an objective designed for water-immersion.



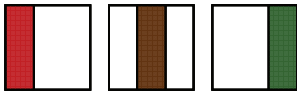
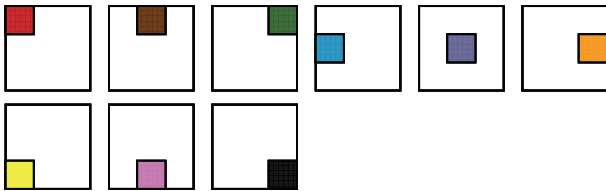
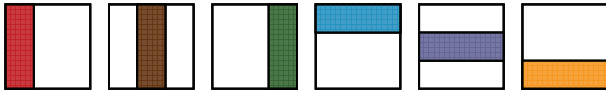
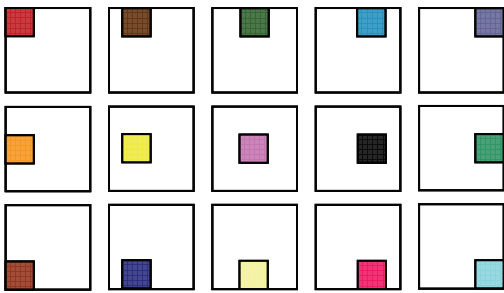
Supplementary Figure 6. Aberration correction for two different fields (**a** and **b,c**) of 500 nm diameter fluorescent beads in air, observed with an objective designed for water-immersion. (**a**) Lateral (X-Y) image after correction of a $96 \times 96 \mu\text{m}$ field of beads. Insets show lateral (X-Y) and axial (X-Z) images of individual beads at different field positions, comparing system aberration correction only with full AO correction, the latter obtained from one bead near the center of the field of view. (**b**) Lateral (X-Y) image of another field of beads acquired with system aberration correction only, and the associated axial Z-Y intensity projection integrated along the lateral X direction. (**c**) Corresponding images of the same beads, using full AO correction. The display gain of the system corrected images is increased $7\times$ in (**b**) to improve visibility. Rotating integrated intensity projections distilled from the 3D image stacks for the system correction and full AO correction are shown in **Supplementary Movie 3**.

Supplementary Figure 7 Quality of aberration correction versus the number of corrective subregions N .



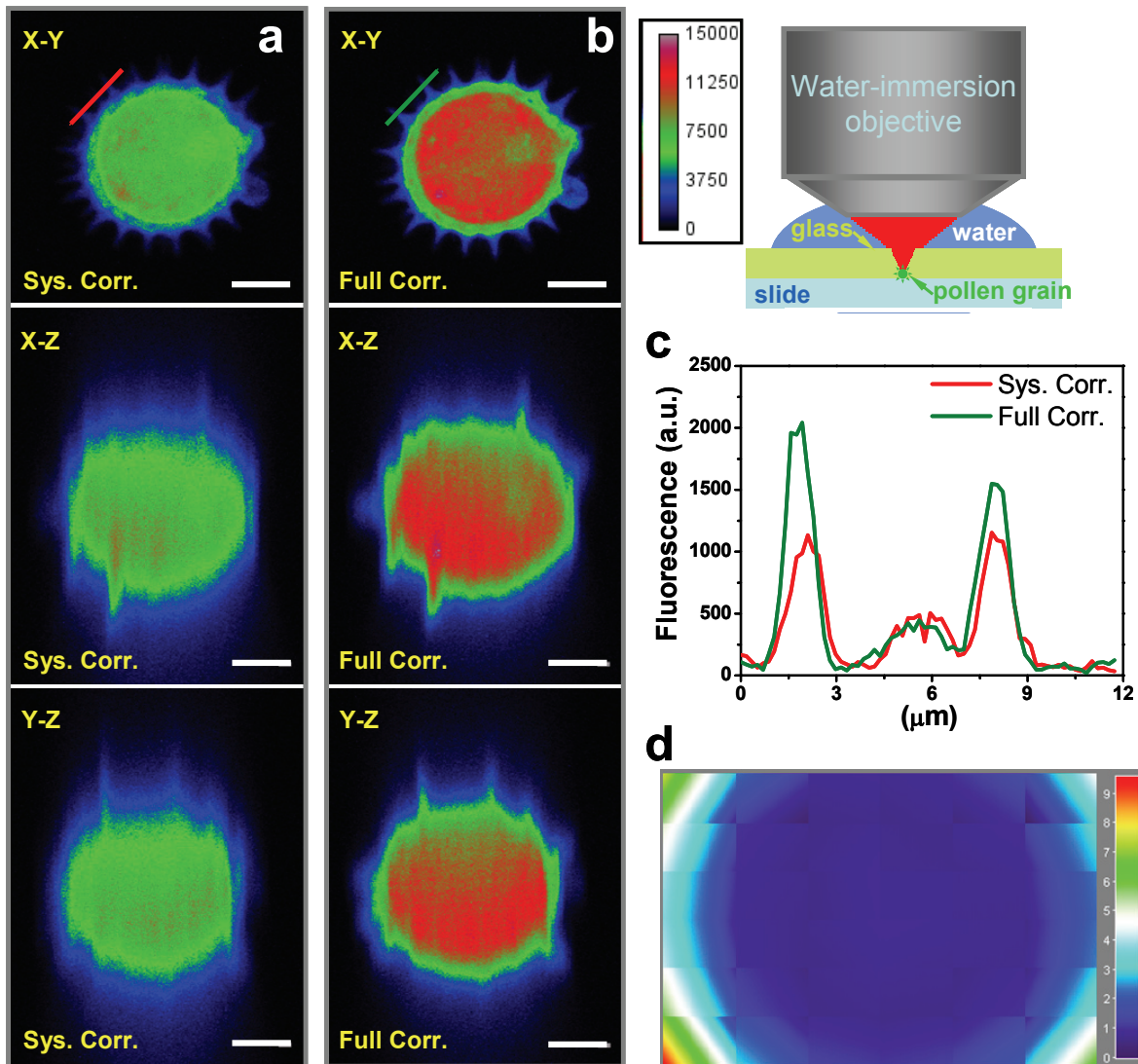
Supplementary Figure 7. (a) Lateral (top) and axial (bottom) images of a 1 μm bead as viewed through 250 μm thick fixed mouse brain slice under different correction conditions as noted. (b) Lateral and axial full width at half maximum and peak signal for each of the correction conditions in (a). (c) The final corrective wavefront in units of wavelength λ ($\lambda = 850\text{nm}$), after subtraction of system aberrations, for the cases $N = 12$, $N = 16$, $N = 20$, and $N = 25$, obtained using the independent mask algorithm with direct phase measurement. Scale bar: 2 μm .

Supplementary Figure 8 Comparison of the independent, overlapping, and stepped overlapping mask approaches to AO correction.

Mask Summary	Set of Masks	Pupil Subregions
a <ul style="list-style-type: none"> • 3x1 Independent Masks, • N = 3 subregions • Each mask: 1/3 pupil area, corresponds to 1 subregion 		
b <ul style="list-style-type: none"> • 3x3 Independent Masks, • N = 9 subregions • Each mask: 1/9 pupil area, corresponds to 1 subregion 		
c <ul style="list-style-type: none"> • Overlapping Masks, • N = 9 subregions • Each mask: 1/3 pupil area 		
d <ul style="list-style-type: none"> • 3x3 w/ 2x1 Stepped Overlapping Masks • N = 18 subregions • Each mask: 1/9 pupil area 		

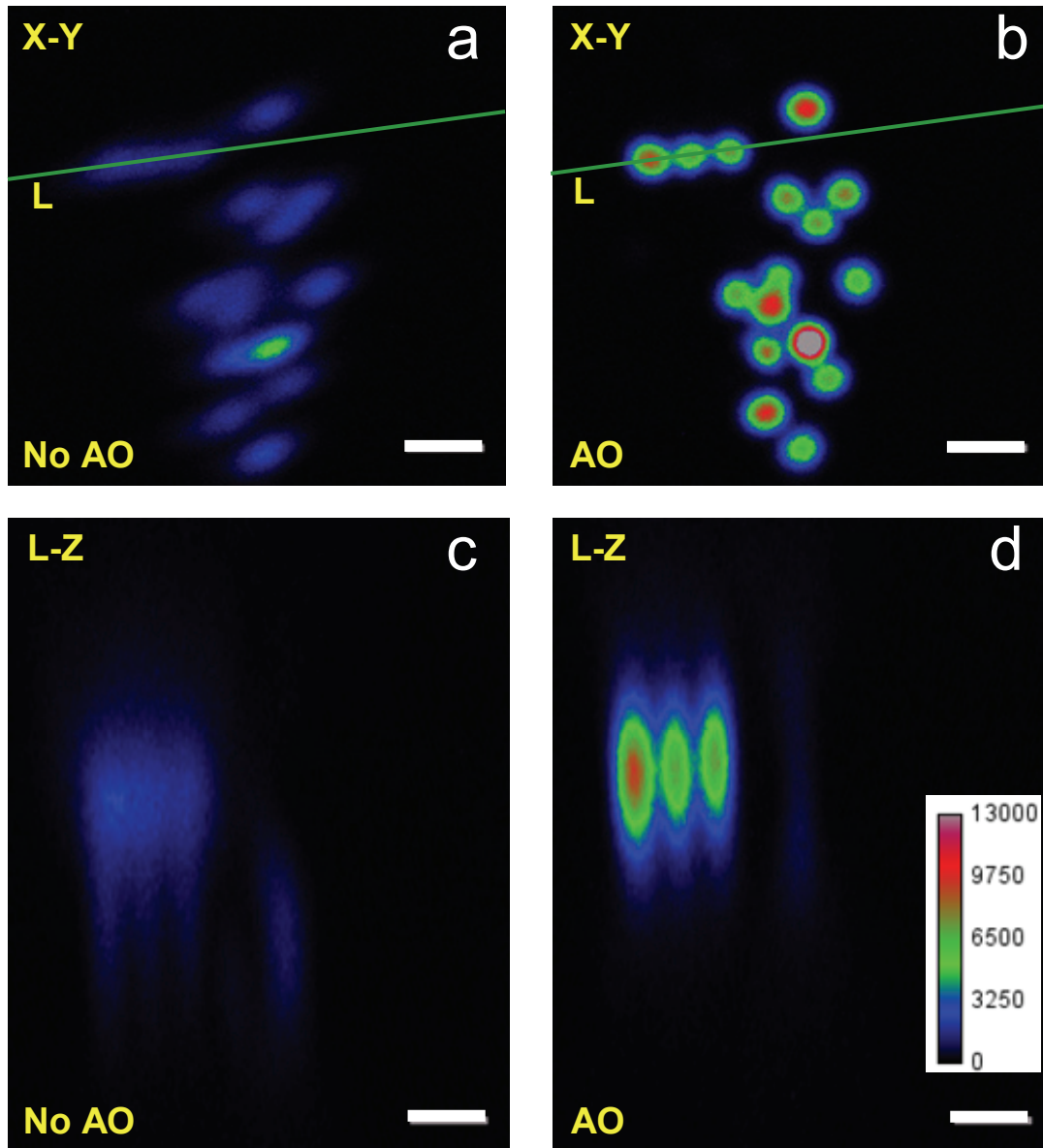
Supplementary Figure 8. Examples of the independent, overlapping, and stepped overlapping mask approaches to AO correction. The objective rear pupil is represented by the large square, and the colored rectangles represent the fraction of the pupil turned on at specific points during beam deflection measurement. **(a)** Independent mask approach: three non-overlapping masks, each covering 1/3 of the total pupil area, independently measure beam deflection in each of three pupil subregions. **(b)** Independent mask approach: nine non-overlapping masks, each covering 1/9 of the pupil area, independently measure beam deflection in each of nine pupil subregions. **(c)** Overlapping mask approach: six overlapping masks, each covering 1/3 of the pupil area, lead to unique wavefront estimations in each of nine pupil subregions. **(d)** Stepped overlapping mask approach: a mask covering 1/9 of the pupil area is translated in horizontal steps equal half the width of the mask, and in vertical steps equals to its height. Beam deflection is measured at each position. The example shown is denoted as 3x3 with 2x1 stepped overlapping masks. See **Online Methods** for detailed explanation.

Supplementary Figure 9 Aberration correction using centroid measurement without reference beads improves images of a fluorescent pollen grain under glass.



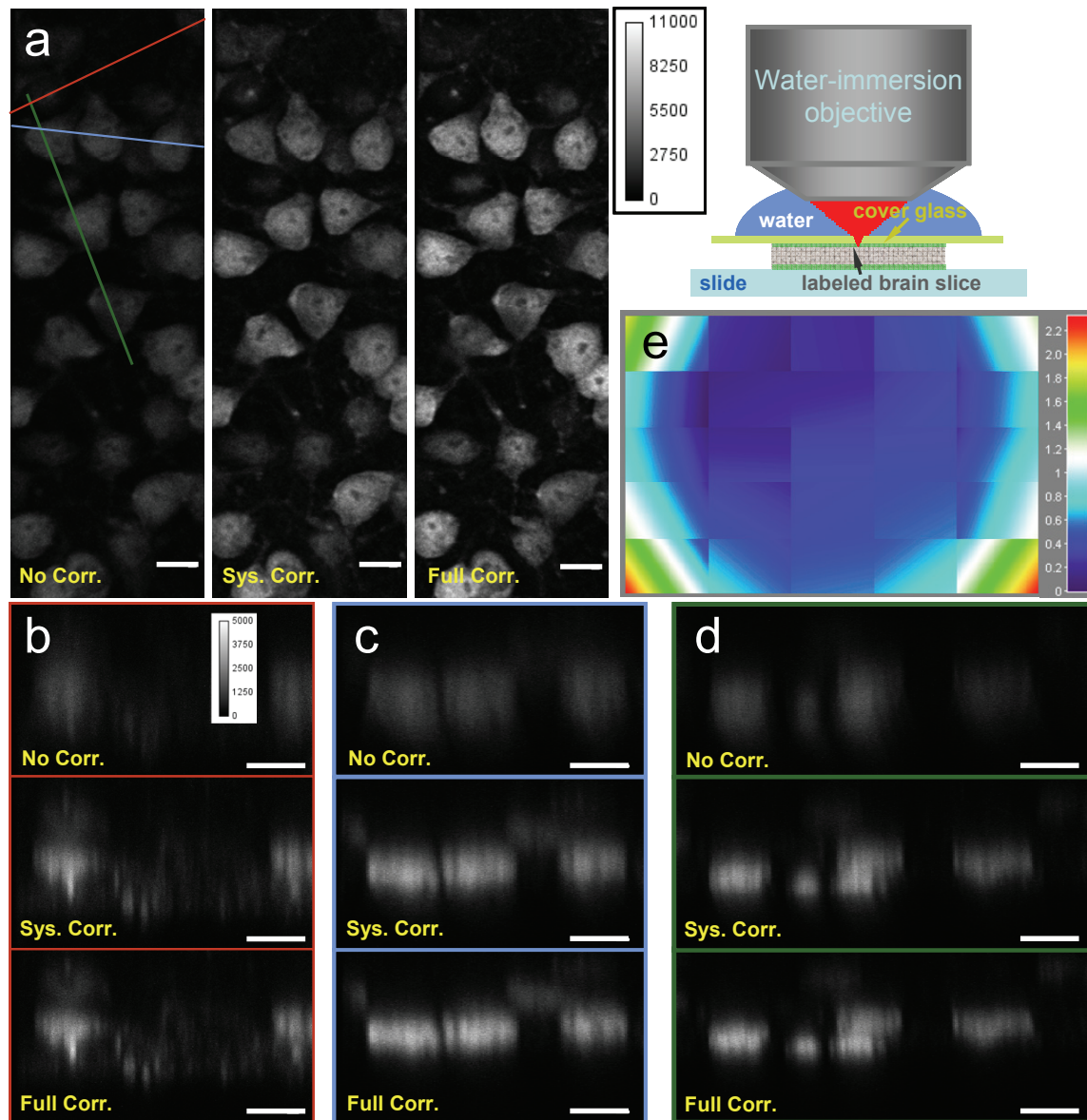
Supplementary Figure 9. Lateral and axial images of a fluorescent pollen grain under four aberration-producing cover glasses (inset), with system aberration correction only (**a**) and full AO correction (**b**). The centroid of the grain itself was used for AO correction, since no reference beads were added. (**c**) Intensity profiles along the colored lines in (**a,b**). (**d**) Final corrective wavefront in units of wavelength λ ($\lambda = 850\text{nm}$), after subtraction of system aberrations, using the independent algorithm with $N = 36$ subregions and direct phase measurement. Scale bar: $10\ \mu\text{m}$.

Supplementary Figure 10 Correction for system aberration using image correlation on a collection of beads in water.



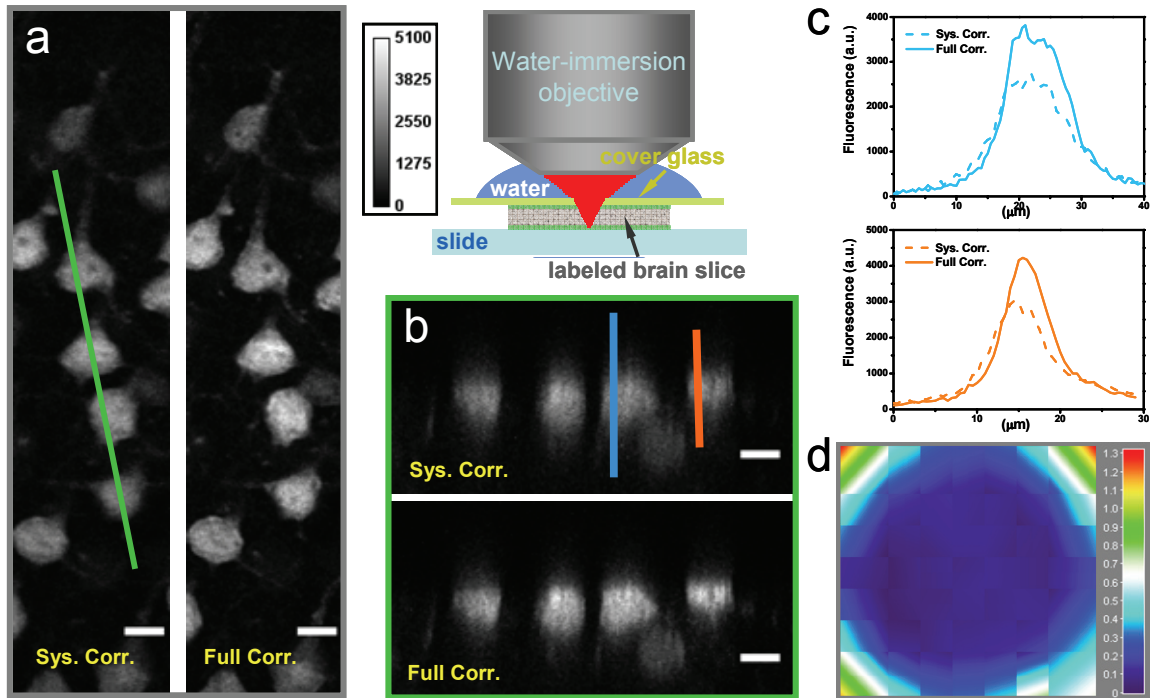
Supplementary Figure 10. (a) Lateral image of a field of 500 nm and 1 μm fluorescent beads in water, obtained with no aberration correction. (b) Same field of beads, after correction for microscope system aberrations, as determined using image correlation. (c) Image without correction, in the axial plane containing the green line in (a). (d) Aberration corrected image, in the same axial plane. Scale bar: 2 μm .

Supplementary Figure 11 Aberration correction at the top surface of an antibody-labeled 300 μm thick fixed mouse brain slice.



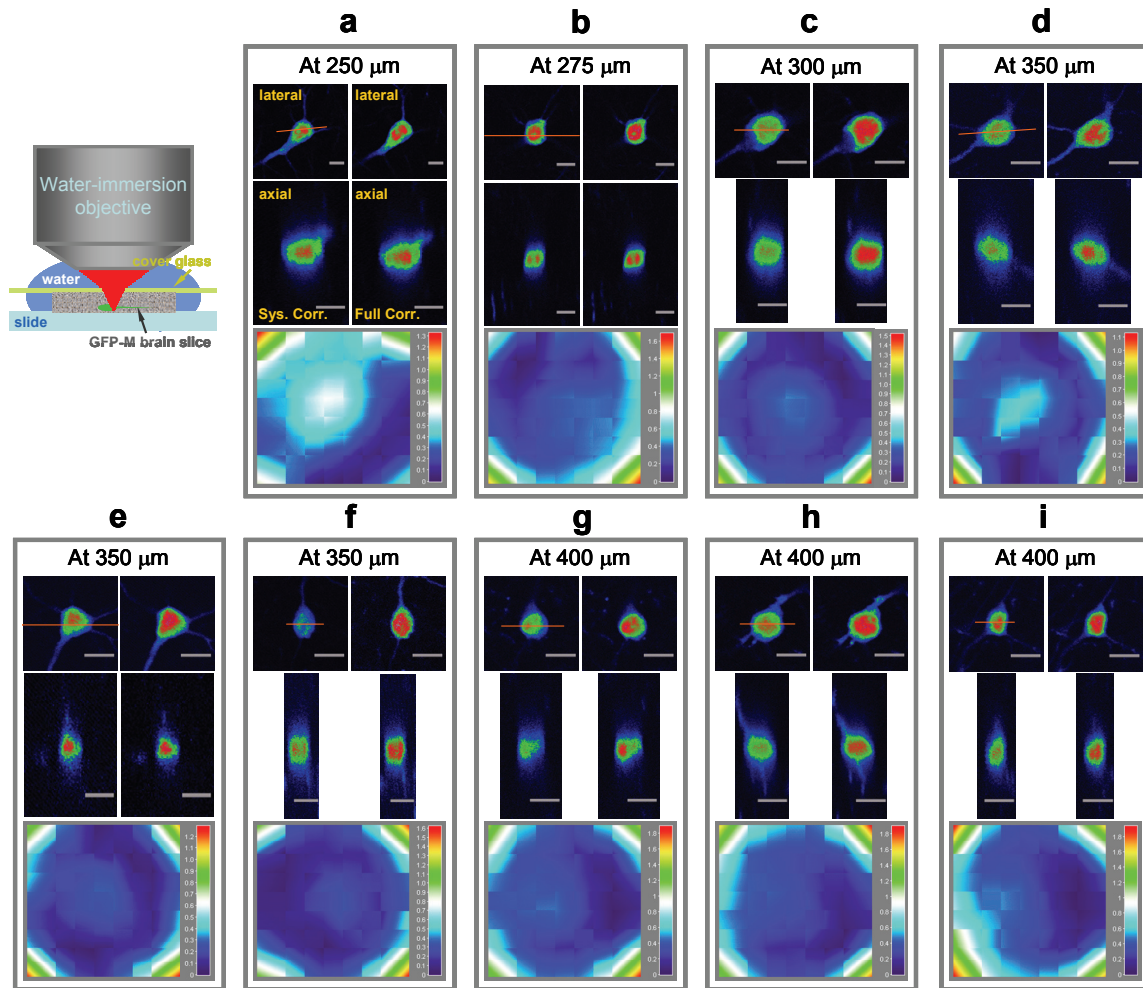
Supplementary Figure 11. Aberration correction at the top surface of a glass covered, antibody-labeled 300 μm thick fixed mouse brain slice (inset, top right), obtained using image correlation for beam deflection measurements. (a) Lateral images of a field of neurons acquired with, from left to right, no correction, system correction only, and full AO correction. (b,c,d) Images in the axial planes defined by the red, blue, and green lines in a, respectively. (e) The final corrective wavefront in units of wavelength λ ($\lambda = 850\text{nm}$), after subtraction of system aberrations, using the independent mask algorithm with $N = 25$ subregions and direct phase measurement. Scale bar: 10 μm .

Supplementary Figure 12 Aberration correction at the bottom surface of an antibody-labeled 300 μm thick fixed mouse brain slice using image correlation and phase reconstruction.



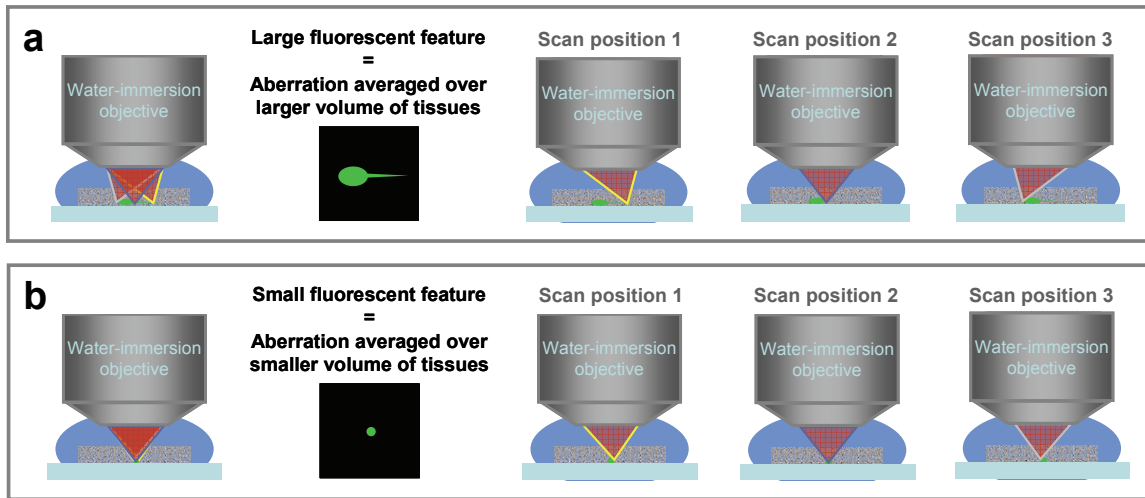
Supplementary Figure 12. Aberration correction at the bottom of a glass covered, antibody-labeled 300 μm thick fixed mouse brain slice (inset, middle), obtained by image correlation and phase reconstruction. **(a)** Lateral images of a field of neurons acquired with, from left to right, system correction only and full AO correction. **(b)** Images in the axial planes defined by the green line in **(a)**. **(c)** Comparative intensity profiles along the blue and orange lines in **(b)**. **(d)** The final corrective wavefront in units of wavelength λ ($\lambda = 850$ nm), minus system aberrations, using the 4x4 with 2x2 stepped overlapping mask algorithm and phase reconstruction. Scale bar: 10 μm .

Supplementary Figure 13 Aberration correction of GFP-labeled neurons at different depths below the surface of fixed mouse brain slices using image correlation and phase reconstruction.



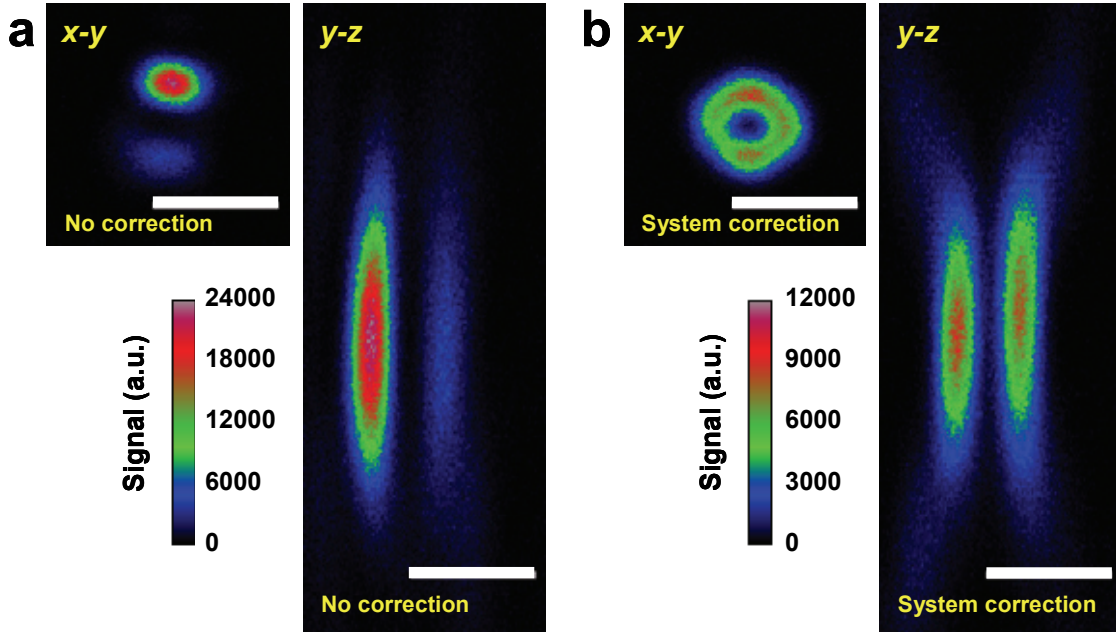
Supplementary Figure 13. Aberration correction of GFP-labeled neurons at (a) 250 μm, (b) 275 μm, (c) 300 μm, (d) 350 μm, (e) 350 μm, (f) 350 μm, (g) 400 μm, (h) 400 μm, and (i) 400 μm below the surface of fixed mouse brain slices, as obtained using image correlation. At each depth, lateral and axial images of the target neuron are shown with system correction only and full AO correction, as well as the corrective wavefront in units of wavelength λ ($\lambda = 900\text{nm}$) (after subtraction of system aberrations). The 4×4 with 2×2 stepped overlapping mask algorithm and phase reconstruction was used in each case. Scale bar: 10 μm.

Supplementary Figure 14 Sketches showing the relationship between size of the field over which AO correction is performed to the volume of tissue over which the correction is averaged.



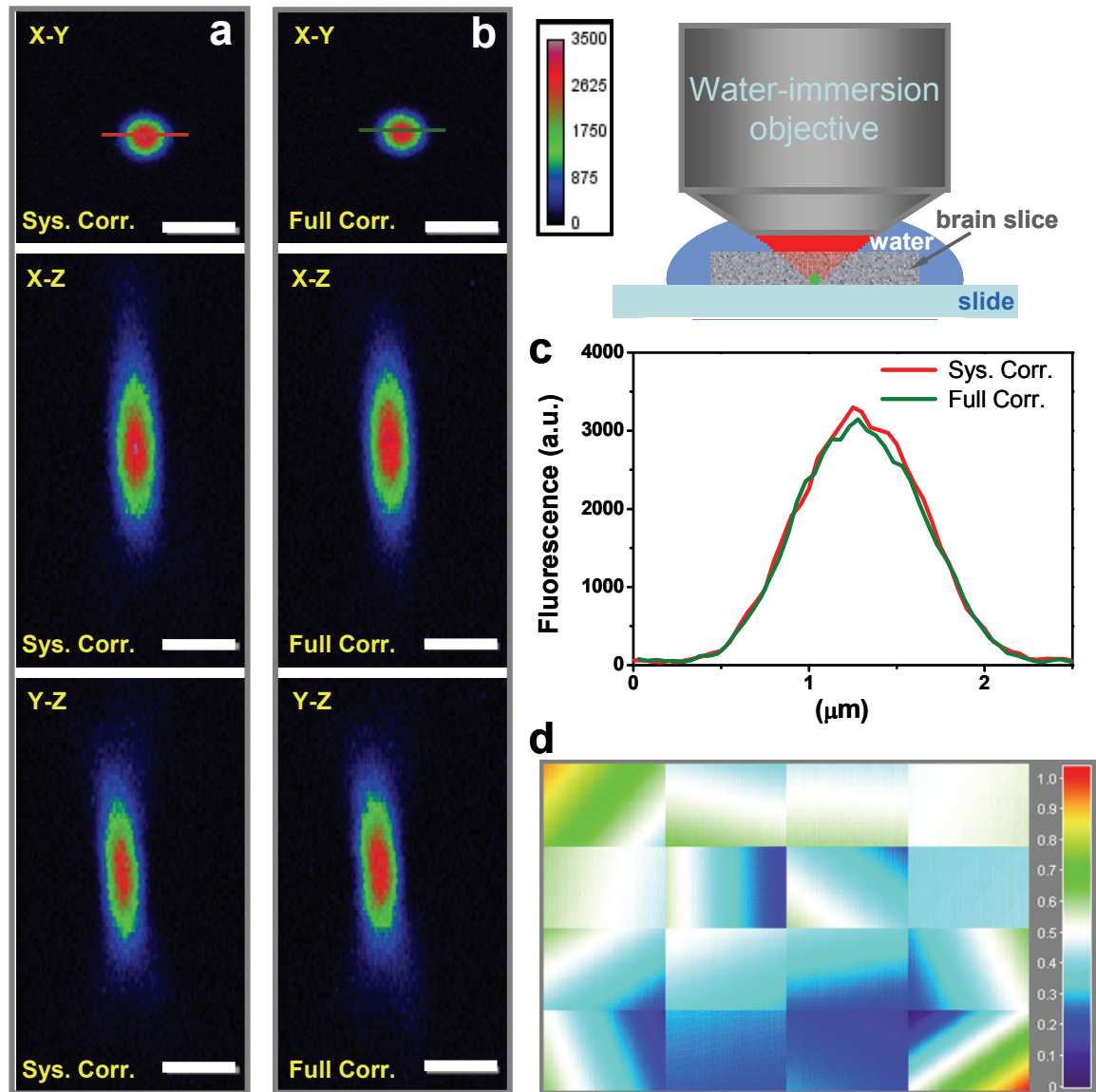
Supplementary Figure 14. (a) When fluorescent features spread over a large field of view are used for AO correction, the excitation beam probes a large volume of biological tissue during correction: the distinct locations of the excitation light inside the tissue at scan positions 1, 2, and 3 show that the measured aberration will represent an average over this large volume. (b) When AO correction is performed over a small field of view, the excitation light probes the same, smaller tissue volume at all scan positions, leading to a correction which is more accurate locally, but may be less accurate elsewhere than the wider, field averaged correction.

Supplementary Figure 15 Effects of system aberration and AO correction of same on the generation of an annular PSF such as is used in stimulated emission depletion microscopy.



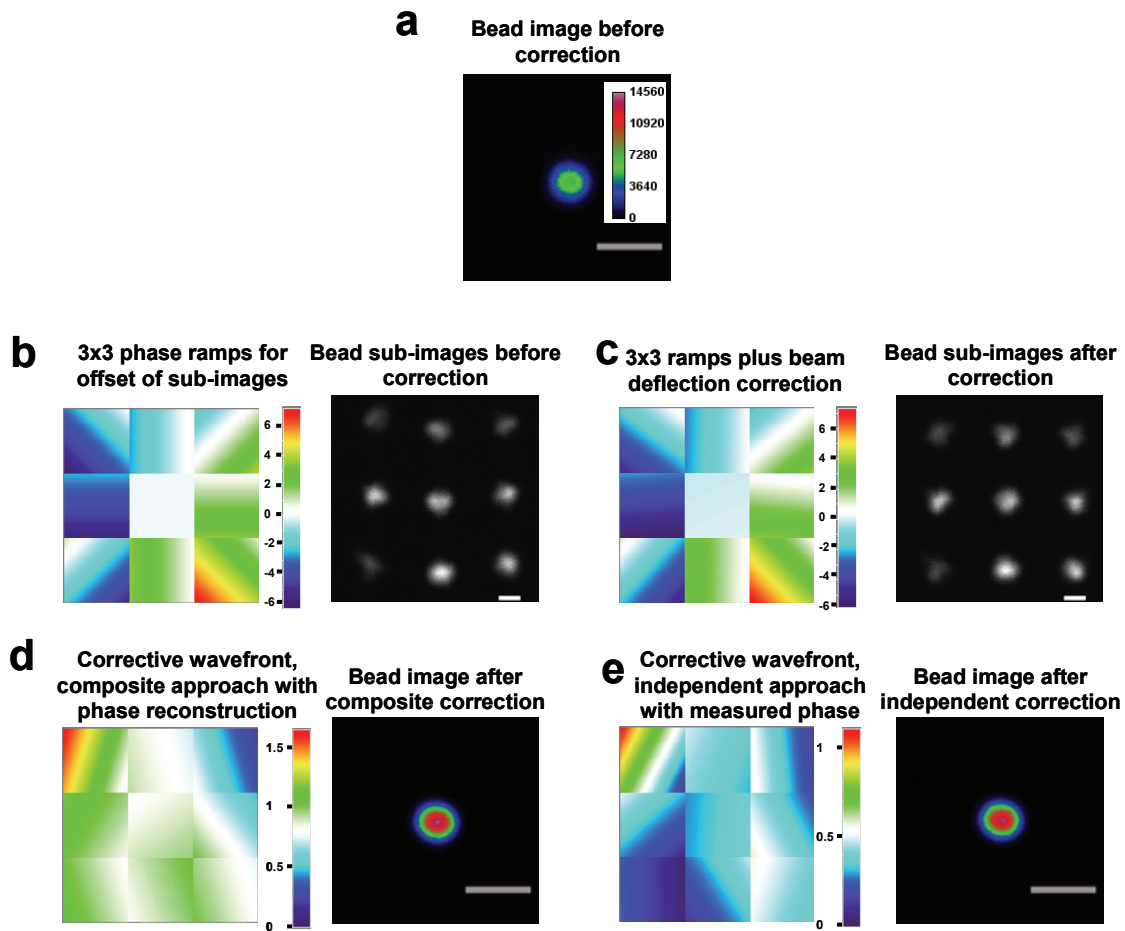
Supplementary Figure 15. Generation of an annular PSF (a) without and (b) with correction for system aberration. Lateral (*x-y*) and axial (*y-z*) images of a single 500 μm diameter bead were taken with a helical phase ramp from 0 to 2π on the SLM. With no aberration correction (a), the resulting PSF was severely distorted; with system aberrations corrected (b), the desired annular PSF with minimal central intensity was obtained. Scale bar: 2 μm .

Supplementary Figure 16 An example of aberration correction through a 250 μm brain slice that did not detect significant aberration.



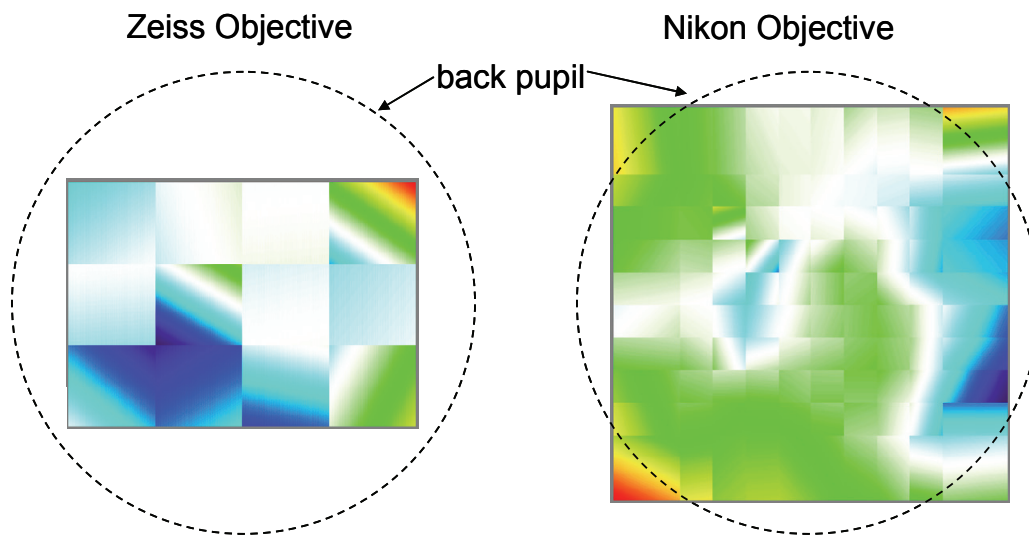
Supplementary Figure 16. Lateral and axial images of a single 1 μm diameter bead under a 250 μm fixed brain slice (inset) with system correction only (**a**) and full AO correction (**b**). (**c**) Intensity profiles along the colored lines in (**a**,**b**). (**d**) Final corrective wavefront in units of wavelength λ ($\lambda = 850\text{nm}$), after subtraction of system aberrations, using the independent algorithm with $N = 12$ subregions and direct phase measurement. Scale bar: 2 μm .

Supplementary Figure 17 AO correction of system aberration using only a single composite image.



Supplementary Figure 17. AO correction for system aberration using only a single composite image. (a) Image of a 1 μm bead when no correction for system aberration was applied to the SLM. (b) After simultaneously applying different phase ramps to each of the 3 \times 3 subregions of the SLM, nine spatially offset sub-images of the same bead were seen. The deviations from the ideal 3 \times 3 array that would exist in the absence of aberration indicate the aberration-induced tilt error that exists in each subregion. (c) Correcting these tilt errors causes the bead sub-images to become aligned with the ideal 3 \times 3 array. (d) The final corrective wavefront obtained using the tilt error data and phase reconstruction, and the resulting corrected bead image, both of which were similar to those obtained by 3 \times 3 independent masks and direct phase measurement (e). Scale bar: 2 μm .

Supplementary Figure 18 Dimensions of the SLM relative to the back apertures of the Zeiss and Nikon objectives.



Supplementary Figure 18. The active area of the SLM relative to the back apertures (dashed circles) of the Zeiss (left) and Nikon (right) objectives.